nature physics

Article

https://doi.org/10.1038/s41567-022-01903-6

Ultrafast relaxation of lattice distortion in two-dimensional perovskites

In the format provided by the authors and unedited

This PDF file includes:

Supplementary discussions 1-11
Figs. S1 to S26
Table S1 to S2
References

Table of Contents

Supplementary discussions 1 - 11

Supplementary discussion 1. Crystal orientation of DJ n=2, DJ n=3, RP n=2 and RP n=4 crystals

The crystal orientation of each sample measured in UED was acquired by comparing the diffraction patterns with the simulated diffractions viewing at different directions.

For the DJ systems, the experimental patterns in Fig. S2b (DJ n=2) and Fig. S13b (DJ n=3) show great consistency with the simulated ones (Fig. S2a & Fig. S13a) viewed at stacking axis direction ([001] for DJ n=2, and [100] for DJ n=3), confirming the horizontal orientation of the DJ crystals, where the perovskite crystal layers are parallel to the substrate. The azimuthally integrated plots (Fig. S2c for DJ n=2, Fig. S13c for DJ n=3) also show good agreement in peak locations and convoluted intensities. The measured in-plane Bragg peaks can be properly indexed accordingly, including (hk0) for DJ n=2, and (0hk) for DJ n=3. The labeled peaks are shown in 2D patterns and azimuthally integrated plot.

For RP n=2 crystal, the simulated pattern along stacking axis [010] is shown in Fig. S20a, where all the peak locations agree with the experimental ones in Fig. S20b, confirming the major orientation of the RP n=2 crystal is horizontal, same as DJ crystals discussed above. Additionally, concentric rings are observed between q=2 $Å^{-1}$ and 3 $Å^{-1}$, as observed in Fig. S20b, suggesting the existence of poly-crystalline like crystal structure with mixed orientations. The azimuthally integrated plots (Fig. S20c) show good agreement in peak locations and convoluted intensities, with additional unassigned peaks at q=2.6 $Å^{-1}$ and 3.7 $Å^{-1}$. We've excluded the possibility of PbI_2 diffraction by comparing with the electron diffraction of PbI_2 thin film.[1] We attribute them to the possible perovskite diffraction from out-of-plane or mixed directions, or an unidentified phase of 2D perovskites, and have excluded them from the discussion of in-plane Bragg peaks responses of RP n=2 crystals.

For the RP n=4 crystal, the simulated pattern along stacking axis [010] is shown in Fig. S21e, with corresponding 1D azimuthally integrated plot in Fig. S21f. However, this pattern doesn't match with the experimental one (Fig. S21a) based on the following observations: 1) more peaks are observed in static UED patterns, such as q=2.2$Å^{-1}$ and 3.8 $Å^{-1}$ as shown in Fig. S21f; 2) anisotropic

intensity distribution along q_x and q_y directions, which is different with Fig. S21e with 4th fold symmetry. Therefore, we conclude the beam direction is not perfectly along the stacking axis as observed in DJ and RP n=2 crystals. As shown in Fig. S21c & Fig. S21d, we find that the [011] orientation gives the best match for RP n=4, with 7.8 degrees deviation from stacking axis [010], as sketched in Fig. S21b. As a result, some out-of-plane Bragg peaks can be detected as well, which may explain the anisotropic UED response between q_x and q_y directions, including the intensity change shown in Fig. S15 and the time constants shown in Fig. S16.

Supplementary discussion 2. Sample Thickness and Carrier Density Estimation

Crystal thickness determination: The thickness of the crystal was determined by comparing the absorbance spectrum with the estimated one calculated from absorption coefficient of 2D perovskites. Here we have referenced the absorption coefficients obtained from ellipsometry by Song et al.[2] Applying Beer-Lambert's law and neglecting light scattering, the relation of crystal thickness d and crystal transmission (T) is given by:

$$T = \frac{I}{I_0} = 10^{-OD} = e^{-\alpha\, d} \tag{S2.1}$$

Where OD is the absorbance in optical density determined by transmission (I/I_0), and α is absorption coefficient. The comparison of experiment and simulated absorbance spectrum is depicted in Fig. S1.

Carrier density: The light-injected carrier density in quantum well is estimated by:

$$n_0 = \frac{\Phi/(h\nu)\, A}{d/l_w} \tag{S2.2}$$

Where Φ stands for energy fluence of each pulse (mJ/cm^2), $h\nu$ stands for excitation phonon energy (3.1 eV for UED), A stands for absorbance of the sample, d is the sample thickness, and l_w is the width of quantum-well in 2D perovskites.[3,4] Here, we've neglected the sample reflection and estimated the sample absorbance by transmission data in Fig. S1. As a result, the list of thickness and corresponding carrier densities of each measurement is shown in Table S1.

Supplementary discussion 3. Time constants of Bragg peaks of DJ and RP crystals.

A. *DJ perovskites*

Time traces of the Bragg peak families of DJ n=2 are shown in Fig. S3, with rapid rise (τ~1ps) in {400}, as well as slower decay (scale of 5ps) of the other major group families. List of fitted intensity change (Δ (%)) and time constant (τ) of each Bragg peak (hk0) is listed in Fig. S7. Both the intensity changes and time constants show a significant anisotropy with respect to directions in the DJ n=2 crystals, which reflects the lack of a tetragonal axis in the monoclinic centered structure (space group Cc n°9) of the crystals at rest because of the geometry and structure of the 4AMP cation. We also note that the intensity traces of some Bragg peaks such as {330} and {550} show a long recovery time (τ>30 ps, Fig. S3a), which could be related to other heat transfer mechanisms and phonon-phonon interactions.[5]

The responses of time scales are similarly observed in DJ n=3, including a fast rise in {040} (Fig. S13), and similar distribution of time constants for other Bragg peak families (Fig. 4d, corresponding scatter plot shown in Fig. S18).

B. RP perovskites

As suggested in Fig. 4d, comparison of the histograms of the time constants τ for DJ n=2, DJ n=3, and RP n=4 shows a generally slower response (up to 15 ps) for RP perovskites as compared to the DJ crystals. Besides, different dynamics are observed for (400) peaks in RP (Fig. S13).

The slow response time in RP systems can arise from the differences in the lattice softness between the BA and the DJ 2D perovskites. The BA molecules reduce the rigidity of the 2D lattice by comparison to the DJ case, leading to an enhancement of the lower-energy part of the vibrational density of states.[6] It was indeed shown experimentally to enhance the deformation potential mechanism in BA compounds, leading to carrier trapping.[7] This results is also consistent with a recent study on high-resolution resonant impulsive stimulated Raman spectroscopy,[8] showing that the vibrational relaxation in monolayered bromide perovskites relatively fast with flexible alkyl-amines.

Supplementary discussion 4. Possible reasons of Bragg peak increase in DJ perovskites.

In this section, we discuss several possible mechanisms that can cause an increase in the Bragg peaks, such as phase transition,[9] and multiple scattering in monocrystalline samples.[10] No signature of phase transition is found in DJ n=2 perovskites, and we exclude possible effect of by the estimation of extinction distance under MeV electron beams, which is much larger than the sample thickness.

A. *Phase transition from thermal lattice heating.* One of the possible mechanisms that induces the collective lattice ordering in DJ perovskites is the thermally induced phase transition from local lattice heating. To investigate the thermal response of DJ n=2 crystals, we first estimate the temperature jump induced by the laser pump, then using the differential scanning calorimetry (DSC) and temperature dependent XRD results to exclude the possible phase transition effect.

a. *Estimation of temperature jump.*

The local lattice temperature increase is estimated by total input pump energy and samples' specific heat. For DJ n=2 crystals, a carrier density of 2.5×10^{13} cm^{-2} corresponds to a bulk carrier concentration of $n=1.4\times10^{20}$ cm^{-3}, which induces total energy into the lattice:

$$\Delta E = n \times \left(E_{pump} - E_g\right) = 1.4 \times 10^{20} \times (3.1 - 2.2)\ eVcm^{-3} = 20.16\ J/cm^3 \quad \text{(S4.1)}$$

The mole of the DJ n=2 crystal is calculated from crystal structure (4 molecules per unit cell):

$$m = \frac{1}{V_{UC}} \times \frac{4}{N_A} = 2.53 \times 10^{-3} mol/cm^3 \quad \text{(S4.2)}$$

The specific heat of DJ n=2 at T~300K is estimated from DSC measurement, as shown in Fig. S9:

$$C_p = 0.54\ J\ K^{-1}g^{-1} = 728\ J\ K^{-1}mol^{-1} \quad \text{(S4.3)}$$

And the corresponding estimated temperature jump is:

$$\Delta T = \frac{\Delta E}{m * C_p} \sim 11K \quad \text{(S4.4)}$$

b. *Differential scanning calorimetry (DSC) results*.

To investigate possible thermal phase transition induced by lattice heating, differential scanning calorimetry (DSC) was performed from room temperature to 150℃, as suggested in Fig. S9. From the DSC curve, no significant phase transition is observed. Based on over estimation of temperature increase induced by light (SI discussion 6), the local temperature increase in the crystal lattice is below the 15K and no possible phase transition is observed or reported in this range.[11] Therefore, we conclude the collective lattice ordering in light-induced in ultrafast scale, instead of thermally induced caused by lattice heating.

c. Temperature dependent XRD.

Additionally, we performed temperature XRD from room temperature to 55°C, data shown in Fig. S10. As we can see, most of the Bragg peak intensities go through a slight decrease with increasing temperature due to the presence of Debye Waller effect.

Here we focus on the in-plane Bragg peaks, primarily related to the edges and diagonal of the perovskite octahedral, which is our main focus in-plane diffraction patterns in DJ n=2. Fig. S10 (b)(c)(d) plot the peak profile variation with respect to the sample at room temperature, zoomed at q- regions near (220) and (400) respectively. As we can see, both (220) and (400) peaks exhibit slight intensity decrease, which is contradictory with the UED response.

Besides the intensity variations from observed from temperature XRD, we also observed a global peak shifting (upto 0.15%, Fig. S10 (f)). A global shifting of Bragg peaks toward low-q values is generally expected from the thermal expansion. However, this behavior of Bragg peaks shifting is not resolved in the UED. We attribute the absence of thermal expansion signature in UED diffraction patterns to the low q resolution of the UED measurements (≈0.17$Å^{-1}$).

In fact, the transient increase in the collective ordering in the DJ n=2 lattice may be viewed as an 'incomplete transformation' towards a completely ordered phase. Indeed, no evidence of phase transition is found from differential calorimetry and XRD. Additionally, the perfectly undistorted 2D perovskite reference phase has only been observed in the fully inorganic Cs-based Cs2PbI2Cl2 2D perovskite at room temperature,[12] which emphasize the importance of the anisotropy of the 4AMP organic cations in the structure for the lattice distortion in hybrid 2D perovskites. On the contrary, undistorted phases are common for hybrid 3D perovskite compounds at room temperature and therefore any ultrafast light-induced ordering is lacking.[13]

B. *Multiple scattering effect.* Another possible mechanism would be the possible multiple scattering effect in single-crystalline samples, as reported by Vallejo et al using keV electron beams.[10]. In fact, as pointed out by Vallejo et al, the possibility of having multiple scattering will rely on a characteristic length known as the extinction distance ($\xi_{\mathbf{g}}$) of the samples, which is strongly affected by the electron beam energy, crystal structure and elements of material (Williams & Carter 2008[14]) as described by the following formula,

$$\xi_{\boldsymbol{g}} = \frac{\pi V cos\theta_B}{\lambda F_{\boldsymbol{g}}} \tag{S4.5}$$

Where V is the volume of the unit cell, θ_B is Bragg angle, λ is electron wavelength, and F_g is the structure factor at diffraction vector $\boldsymbol{g}$.

The calculation of V, λ, and θ_B is straightforward. For high energy electrons θ_B is fairly close to 0, since the electron wavelength λ is much smaller than lattice spacing (θ_B=0.5 deg for Si (220) at 100keV) and therefore $\cos\theta_B \approx 1$. The F_g is estimated by the summation of all the atomic scattering factors with different atomic locations within the unit cell (Williams & Carter 2008 [14], Page 223):

$$F_g = F_{hkl} = \sum_{i=1}^{n} f_i^{(e)}\, e^{-2\pi i(hx_i + ky_i + lz_i)} \tag{S4.6}$$

The atomic scattering factor is a function of scattering vector s ($s = \sin\theta\,/\lambda$). and a common approximation is fitted with the following formula[15]:

$$f^{(e)}(s) = \sum_j a_j \exp(-b_j s^2) \tag{S4.7}$$

The coefficients of a_j, b_j for each atoms are listed in Table 1 in Peng et al[15]. For ionized atoms (such as Pb2+ and I-), additional term is included[16].

Based on the information above, we have estimated the extinction distance for Si under 100keV and DJ n=2 perovskites under 3.7MeV, which are given by:

$$\xi_{\boldsymbol{Si}|(\boldsymbol{220})} = \frac{\pi V cos\theta_B}{\lambda F_{\boldsymbol{g}}} = \frac{\pi * \ 163.6\text{Å}^3 * 1}{3.70e-2\text{Å} * \ 15.06\ \text{Å}} = 92\ nm$$
$$\xi_{\boldsymbol{DJ2}|(\boldsymbol{220})} = \frac{\pi V cos\theta_B}{\lambda F_{\boldsymbol{g}}} = \frac{\pi * 2627\text{Å}^3 * 1}{2.97e-3\text{Å} * \ 261.73\ \text{Å}} = 1062\ nm \tag{S4.8}$$

The calculation of Si is close to the value reported in the literature (75.7 nm)[14], giving a fair estimation. Compared to the sample thickness of d≈270nm of DJ n=2 crystal, the extinction distance is ~4 times larger, therefore we believe the multiple scattering effects are not likely to happen in DJ n=2 perovskites.

Furthermore, in order to give a clear demonstration of the absence of multiple scattering, we have simulated the diffraction pattern of DJ n=2 based on kinematic scattering theory following the assumptions of weak-phase object approximation, which is a commonly used to model the crystal diffraction from electron microscopy.[17,18] The calculated pattern for 4 by 4 supercell is shown in Fig. S22. The simulated diffraction in Fig. S22(b) gives a reasonable match to the experimental diffraction of the crystal at rest Fig. S22(a), and are also in consistency with the calculations in Fig. S2(a), which is directly evaluated from the structural factor: $I_{hkl} \propto |F_{hkl}|^2$. Furthermore, the absence of Kikuchi lines in the scattering pattern also suggests lack of multiple scattering (FIG. S22(c)).[19] A quantitive comparison of the linecut of the patterns is also displayed in FIG. S22(d), which gives a reasonable agreement for the intensity distribution of the Bragg peaks, especially at (400), (310) and (220) which shows the most contrast in the differential response (Fig. 2d) and are the most relevant peaks in the discussion of lattice ordering. This consistency indicates the kinematical scattering will be sufficient to describe the diffraction patterns, and the multiple scatterings are negligible.

Supplementary discussion 5. Estimation of antiferro-distortion in 2D perovskites

A. Simplified model involving rigid octahedral rotations.

Fig. S5 shows the simulated diffractions with intrinsic (Fig. S5a) and reduced antiferro-distortion (Fig. S5b), as well as the corresponding crystal structures with different disordering parameter viewed along stacking axis. The top (in-plane) view of 2D perovskite caused by intrinsic in-plane cell doubling is shown in the schematics in Fig. S5c. The tilted angle between adjacent octahedra ($2\theta = 24^o$) is associated with antiferro-distortion, forming an initially doubled unit cell of 8.8 Å (indicated in red squares), as opposed to the undistorted structure ($\theta = 0^o$) where unit cell is of 6.2 Å (labeled by green squares). To estimate the influence on crystal structure with reduced antiferro-distortion, we've constructed a hypothetic structural phase (Fig. S5d), where interlayer octahedra are more aligned and simulated an electron diffraction pattern correspondingly (Fig. S5b). For a direct comparison between the symmetrized and the intrinsic antiferro-distorsive phase, a subtracted diffraction pattern is displayed in Fig. 2c. As we can see, the intensity variations are expected in specific Bragg planes, including {400} and {220} (bright red) increasing and {310} and {530} (blue).

To estimate the light-induced rotation angle $\Delta\theta = \theta' - \theta_0$, we calculated the percentage of Bragg peak intensity variation as a function of tilting angle (Fig. S5e), and compare them with the experiment data at early time (t = 2ps). From the responses of {310}{400}, we estimated the optimal order parameter to be $\theta = 11.75^o$, as shown in the shadow region in Fig. S5e, corresponding to an octahedral tilt of $\Delta\theta = 0.25^o$.

B. Phonon mode simulations on DJ n=2 crystals.

Besides the simplified model involving pure rigid tilting of octahedra, we believe a more complex model should involve a shift of crystal structure along the eigenvectors of specific normal modes. Therefore, we perform DFT computations on DJ n=2 (Phonon Simulation methods) and suggest several possible vibrational modes candidates, as well as the related diffraction plots, which are listed in Fig. S6. These normal modes are indeed related to the antiferro-distortions (Fig. S6a, c, &e), and shifting the crystal structure along these eigenvectors result in a positive change along {220} and {400} directions, consistent with

the prediction in section A. Therefore, these calculations further confirmed our hypothesis on lattice ordering (Fig. 2).

Supplementary discussion 6. Transient absorption spectroscopy of DJ n=2 crystal and carrier temperature extraction.

The transient absorption (TA) measurements are performed on nearly identical 2D perovskite crystals (similar lateral size L≈200um, thickness d≈300nm and composition (DJ n=2) as used for UED). We used an optical pump set at 3.1 eV (same as UED) with 0.1-0.75 mJ/cm^2 (1.1×10^{12} cm^{-2} - 8.4×10^{12} cm^{-2}, corresponding to an excitation regime similar than in the UED measurements), followed by a white-light probe monitoring the transmission variations of the sample (see Method Section on transient absorption spectroscopy). Therefore, for similar optical pump conditions, we had access to an optical probe in TA, yielding complementary information with respect to the structural ones provided by the UED experiment. The results are displayed below in Fig. S11.

From our TA data, several major observations are summarized:

A. Strong bleaching of exciton states. Fig. S11 (c) shows absorbance spectra at different fluences. We observed a significant bleaching of the exciton peak at 2.18eV monotonically increasing with excitation densities upto 0.75 mJ/cm^2. From our TA studies extrapolated to a fluence of 1-2 mJ/cm^2, we will expect an almost complete bleaching of the exciton resonance leading essentially to a hot electron-hole pair plasma just after the pump in the UED experiment. Furthermore, Fig. S11(f) shows a long lifetime ($\tau\sim10^2$ps) of exciton dynamics, indicating a high density of carriers is still bleaching the exciton resonance over long time, consistent with the observed long lifetime of lattice response in UED.
B. Hot-carrier cooling dynamics. As indicated in Fig. S11 (b), at 0.75 mJ/cm^2, we have observed the cooling phenomenon starting at t~0.4 ps, which is consistent with the typical values reported in halide perovskites.[20,21] We estimated the evolution of the effective carrier temperature after t~0.5ps by fitting the high-energy tail near the band edge with a Maxwell-Boltzmann distribution (Fig. S11 (b)), which is a commonly used method to approximate the carrier temperature in semiconductors.[22] As estimated in Fig. 3(c), the first cooling process of hot-carriers ranges from sub-ps to 1 ps. The initial carrier temperature

is fitted to be $T_c \approx 3700$K for 0.75 mJ/cm^2. We extrapolate this value to be 3300K for a fluence of 1 mJ/cm^2 in the UED experiment.

C. Long-lived coherent acoustic waves. As shown in Fig. S12, we observed a low-frequency oscillations from TA data, which is related to coherent acoustic waves. Through Fourier transform in frequency domain, (Fig. S12(b)), we identify one phonon mode at 0.022 THz (0.09meV), related to temporal period of 45 ps, and are consistently observed for all the measured fluences (0.1-0.75mJ/cm^2). The activation of coherent acoustic modes with >100 ps lifetime suggest a long equilibration time of the phonon bath, on a time scale consistent with the long lifetime of the lattice response in UED.

These TA results suggest that hot electron-hole plasma may be more dominant at this high excitation densities, where many-body interactions and other non-linear processes could play a crucial role, contradictory to the work of Thouin et al. where the excitonic regime is mainly discussed.[23] This conclusion is also confirmed by the quantitate analysis defining the excitation regime and carrier saturation densities vs temperature which are shown below in discussion 7.

In addition to

Supplementary discussion 7. Estimation of saturation densities in DJ n=2 and RP n=2 crystals

We've estimated the carrier temperature in 2D perovskites to be $T_c \sim 3300$K for 1mJ/cm^2. (Discussion 6). The next step consists in computing the saturation densities for the excitonic resonances in the DJ n=2 compound. For that purpose, the binding energy and the Bohr radius of the 1S exciton resonance are considered.[24] It is usually considered that the binding energy is reduced in DJ compounds by comparison to RP ones for the same n, but precise experimental data are not available for DJ n=2. We started from the known values available for RP n=2:[25] $E_{,b,RP}$=245meV for the binding energy and $a_{B,RP}$=1.60 nm for the effective Bohr radius related to the diamagnetic shift. Next, the effect of the smaller interlayer spacing is estimated using the effective dielectric model of Ishihara et al[26] $\varepsilon_{eff,RP}$=4.9 vs $\varepsilon_{eff,DJ}$=5.5, leading in turn to a reduction of the binding energy $E_{b,DJ}$=204meV. The BSE model[25] was then used to compute the diamagnetic shift and finally a $_{B,RP}$=1.56 nm. A summary of saturation densities at different carrier temperate is plotted in Fig. 3e.

Supplementary discussion 8. Generalizability of lattice response and order parameter on 3D perovskites.

In this section, we compare the distinct ultrafast lattice dynamics of different perovskite systems, and discuss the generalizability of other parameter in 3D perovskites. We believe the initial antiferrodistorsive states are indeed important, not only for 2D perovskites but also for the 3D perovskites. The antiferro-distorsive octahedral rotation angles of both 2D and 3D perovskites systems are listed in table S2.

A. 3D iodine perovskites ($MAPbI_3$)

Wu et al have performed the same UED measurements on the polycrystalline thin film of $MAPbI_3$.[1] The behavior of the Bragg peaks is Debye-Waller like, and no similar response involving reduction of antiferro-distortion has been observed. Here, in order to examine the generalizability of the order parameter in 3D perovskites, we have performed a similar simulation with a hypothetic octahedral rotation model (similar as the one described in the manuscript Fig.2), and compare the expected variations of diffraction intensities to the experimental curve from Wu et al. The comparison is shown in Fig. S23.

As shown in Fig. S23, the reduction of the antiferro-distorsion present in the tetragonal phase of $MAPbI_3$, should lead to positive intensity variations at q=2.0 and 2.8Å-1, similar to the ones observed for DJ n=2 (Fig. 2d) as a result of reduced in-plane octahedral rotation towards higher symmetry phase. Indeed, the characteristic positions of the Bragg peaks related to the perovskite backbone are similar in iodide-based 2D and 3D perovskites, because these compounds share similar lengths for the Pb-I bonds. However, by comparing the simulated differential pattern with the UED results for $MAPbI_3$ from Wu et al, such positive response is not observed in the experimental scattering intensity at different delay times (t=5, 70ps), as indicated in Fig. S23(a). In fact, we note that MAPbI3 exhibits a similar behavior than RP phases (Fig. 4, also zoomed in at same q region in Fig. S23(b)), especially in RP n=4 which is close to 3D perovskites. We believe that the consistency of negative intensity response in both 2D RP perovskites and 3D perovskites provide clear evidence of the distinct lattice dynamics in 2D DJ perovskites. The initial distortion generated by the presence of di-cations in DJ perovskites instead of mono-cations for RP

perovskites is important, leading to different space groups, interlayer shifts and in-plane octahedra tilts (Mao et al[3]). From that perspective, the perovskite backbone in RP phases is less influenced by the flexible BA cations in the barrier and exhibit tilt patterns similar to bulk $MAPbI_3$.

B. Oxide perovskites ($SrTiO_3$ & $KTaO_3$)

For oxide perovskite systems, pristine $SrTiO_3$ presents a cubic structure at room temperature and goes through an antiferro-distorsive phase below Tc (105K). The phase transition is antiferro-distorsive with an order parameter related to an octahedral rotation ($\phi \sim 2°$ for T = 5K[27]) and a Bragg superlattice reflection. Indeed, Porer et al observed an ultrafast relaxation of antiferro-distorsive phase in Ca: $SrTiO_3$, where alloying with Ca was used to increase Tc (280K) and initial rotation angle. As observed by Porer et al, this ultrafast lattice dynamics, characterized by superlattice diffraction, is consistently observed in the tetragonal phase below the critical temperature, where a non-zero rotation angle is present at equilibrium. This suggests that similar to our work, an initial octahedral tilt is necessary to give rise to the ultrafast dynamics involving relaxation of antiferro-distortion phase.

In general, in oxide perovskites, distortions can be grouped into two categories:[28,29] either antiferro-distortions (e.g. $CaTiO_3$, $SrTiO_3$) related to the octahedral tilt, or ferroelectric distortions (e.g. $BaTiO_3$), where the B-site atom is displaced within surrounding octahedron. The observation of two types of distortions can be explained by the Goldschmidt tolerance factor.[28] In the case of $KTaO_3$, the ferroelectric order parameter, is connected to the off centering of B-site cation.[30] Therefore, we believe that our results on DJ 2D perovskites rather share some similarities with the reduction of antiferro-octahedral rotation in $SrTiO_3$ with photodoping as reported by Porer et al.

Supplementary discussion 9. Comparison of electron-LO phonon coupling with RP and DJ n=3.

To elucidate the strength and coefficients of the electron-LO phonon interactions, we performed temperature-dependent PL on DJ n=3 perovskites, where we monitor the linewidth of PL broadening as a function of temperature. The result is shown in Fig. S24.

The PL of DJ perovskite shows an asymmetric shape with two profiles. Here we focus at the dominant exciton emission at higher energy and plot the FWHM as function of temperature (Fig. S24(b), blue). Such behavior is also compared with RP n=3 (displayed in orange).

Here, the linewidth of DJ perovskites shows an anomalous broadening below 80K, which is similarly resolved in $MAPbI_3$ system[31], and is most likely also related to the influence of a phase transition in this temperature range. However, far above 80K in a temperature range relevant for the discussion of the present work, the broadening in DJ perovskites is consistent with the one in RP perovskites. It suggests that the strengths of the electron-phonon coupling in DJ n=3 and RP n=3 perovskites are not significantly different at high temperatures, and that the observed lattice ordering in DJ perovskites is not due to a specific electron-LO phonon coupling, which would otherwise cause similar lattice response between RP and DJ perovskites.

Supplementary discussion 10. Estimation of long-time Bragg peak response and light-induced atom RMS displacements $\langle u^2 \rangle$

Due to the deviation of Debye-Waller response (Fig. S25) of DJ n=2 crystal, the Bragg peaks intensity responses show competing effects between the conventional Debye-Waller effect and incipient anisotropic lattice ordering:

$$I_{total}(\vec{q}) = [I_0(\vec{q}) + \Delta I(\vec{q}, \Delta\theta)]\, e^{-\frac{1}{3}\Delta\langle u^2\rangle\, q^2} \quad \text{(S7.1)}$$

Here $I_0(\vec{q})$ stands for the diffraction intensities at rest. The total Bragg peak intensity response have two contributions: i) an initial ordering process represented in $\Delta I(\vec{q}, \Delta\theta)$, where $\Delta\theta$ is the change of distortion angle (shown in Fig. 2b), which is estimated in Supplementary discussion 5. $\Delta I(\vec{q}, \Delta\theta)$ is simulated based on reduction of andiferro-distortion and also shown in Fig. 2c. ii) classical thermal energy transfer involving all the Bragg peaks, represented in Debye-Waller effect as exponential term $e^{-\frac{1}{3}\Delta\langle u^2\rangle\, q^2}$, where $\langle u^2 \rangle$ stands for atomic mean squared (RMS) displacement.

The competing effect of the two mechanisms is also indicated in Fig. S8, where considering only the first contribution (gray dashed line, Fig. S8(b)) will not give a good prediction at long delay time (40-80 ps) especially at higher q, while the combining effect of the two (black solid line) matches better with the experimental response. By comparing the simulated intensity change with

the Bragg peak response at long time, the Debye-Waller factor is estimated to be 1.6×10^{-3} Å^{-2}, corresponding to light-induced atom RMS displacement of $\sqrt{\Delta\langle u^2\rangle}$ ~ 0.07 Å at carrier density of 2.5×10^{13} cm^{-2}.

Supplementary discussion 11. Time evolution of diffraction intensities through the UED run.

Fig. S19 shows the time evolution over ~2 hours during the UED run of DJ n=2 crystal. As shown in Fig. S19a, the total diffraction intensity doesn't show a significant drop over ~2 hours, suggesting the crystal structure remains stable throughout the experiment. Fig. S19b shows the comparison of the electron diffractions between 0min and 120mins, where all the Bragg peaks remain existing, with a slight decrease of overall intensities. Additionally, no rings or new peaks were formed through the experiments (Fig. S19c and Fig. S19d), confirming that no evidence of possible sample degradation or damage is found.

Supplementary Figures S1 – S26

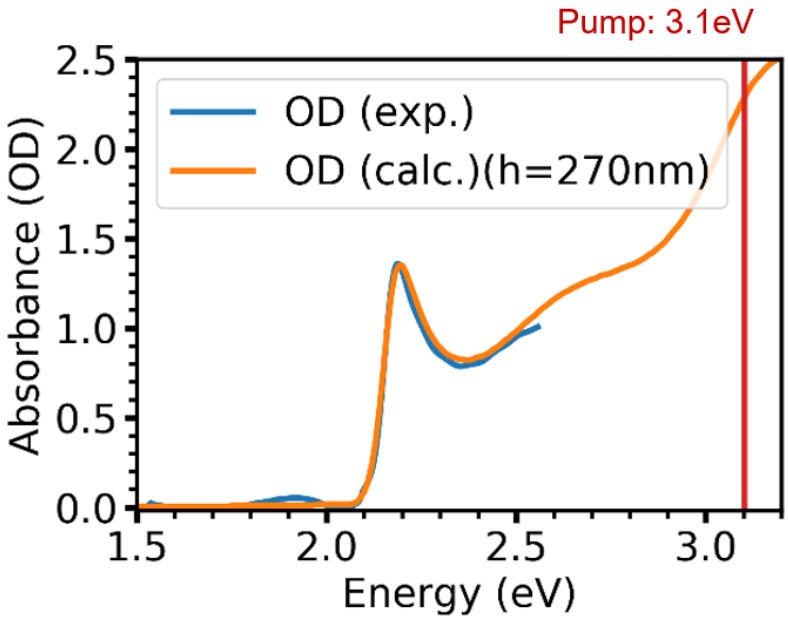

Fig. S1 | Optical absorbance spectra of DJ n=2 crystal. The measured absorbance is shown in blue line, with calculated absorbance (orange line) with crystal thickness of 270nm, estimated from the absorption coefficient as reported by Song et al.[3]

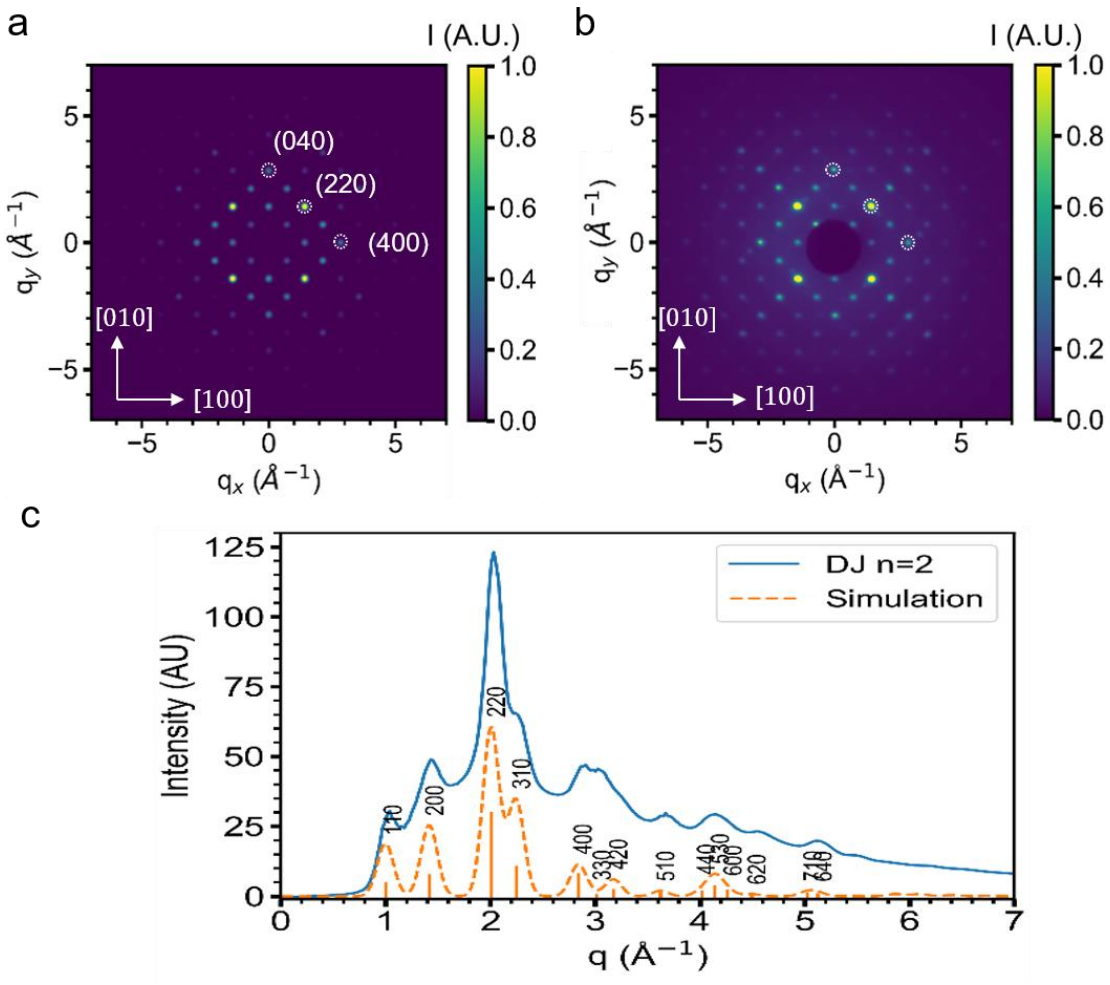

Fig. S2 | Simulated Diffraction Pattern & Indexing of DJ n=2 crystal. (a) Simulated Diffraction of DJ n=2 crystal, viewing from [001] direction. **(b)** Static Diffraction of DJ n=2, showing same q-range as the simulated one in Fig. S2a. All the Bragg peaks are well-identified. **(c)** Angular-integrated diffraction of DJ n=2, showing both experimental (blue solid line) and simulated (orange dashed line) plots, as well as Indexing of Bragg peaks (hk0).

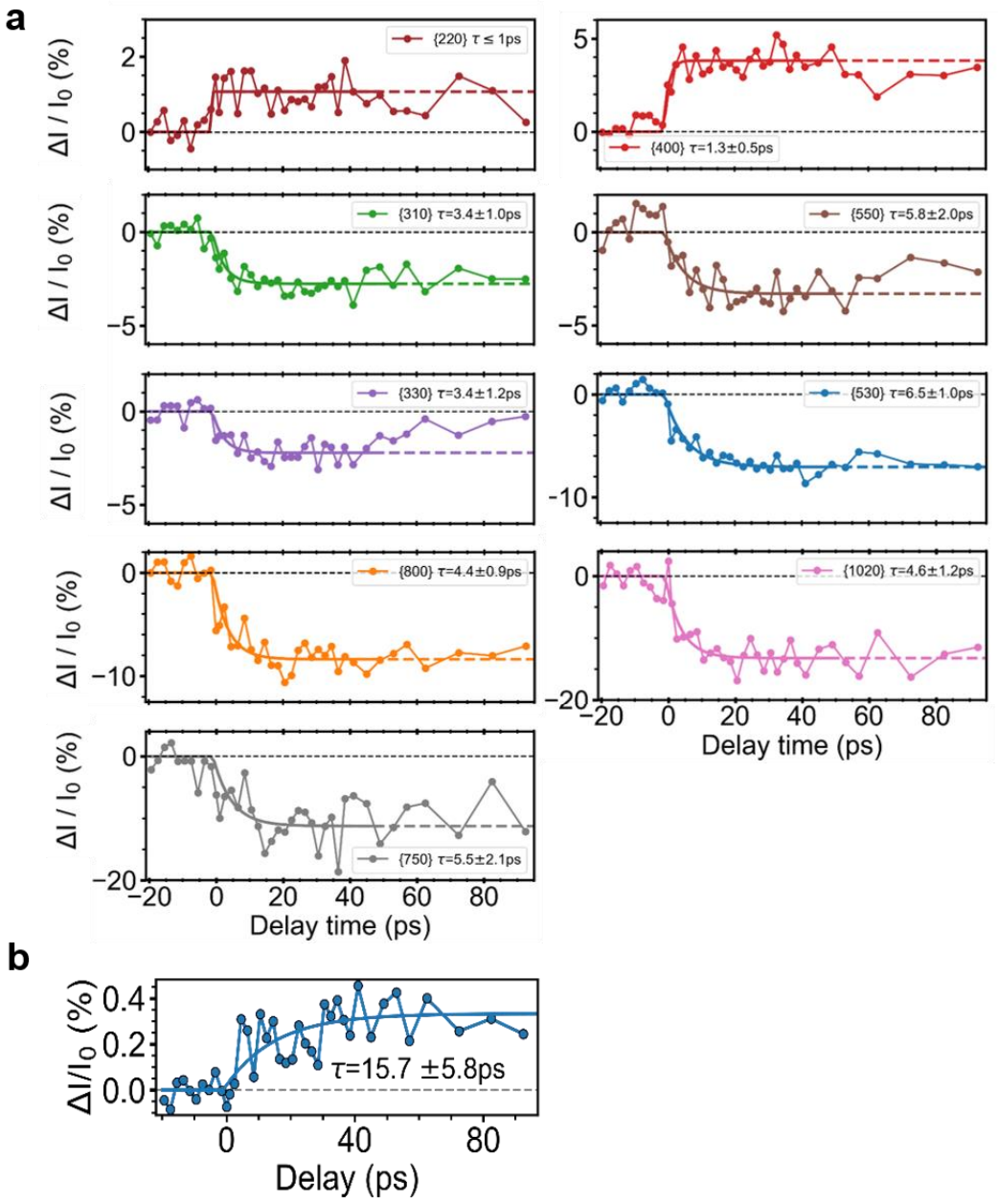

Fig. S3 | Time traces of selected Bragg peak families in DJ n=2 crystal. (a) Time traces of Bragg peaks intensities of {220}{400} {310} {330} {1020} {550} {530} {800} and {750} for DJ n=2 crystal. Errors of time constants are defined as one standard deviation errors estimated from the variance of the fitting parameters from least-squares fitting. The statistics of {220} is not good enough be fitted with a reasonable time constant. We estimate the time scale to be ≤1ps limited by temporal step size. **(b)** Dynamic plots of the total integrated diffuse scattering intensities between Bragg peaks.

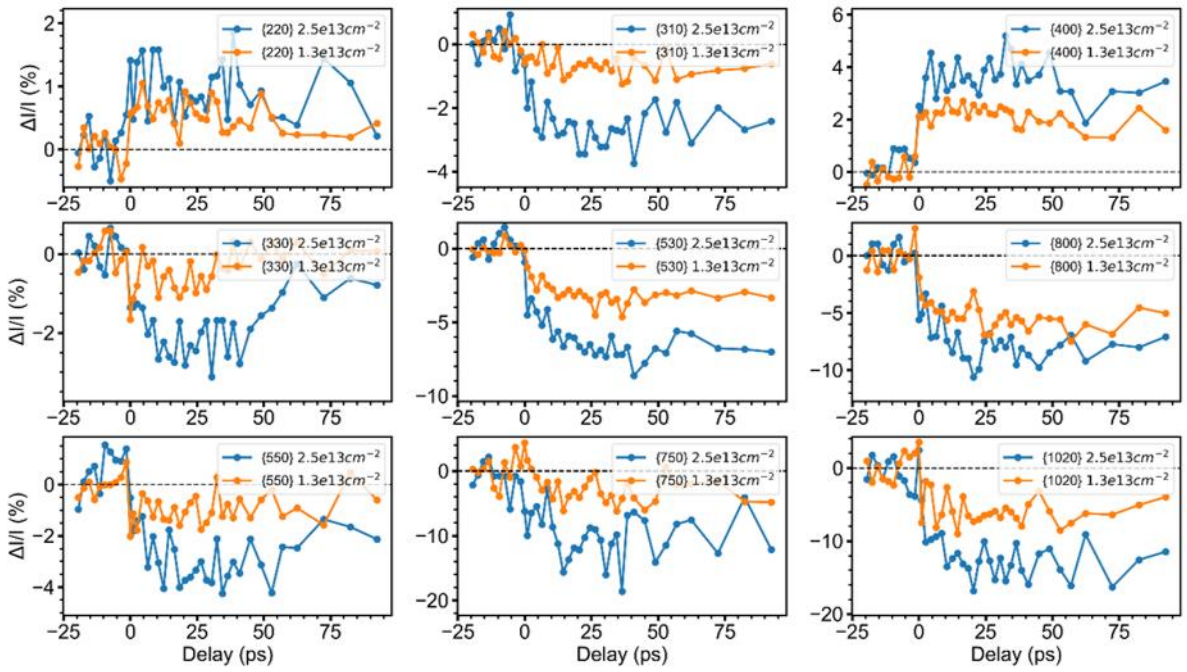

421

422 **Fig. S4 | Fluence dependence for selected Bragg peaks in DJ n=2 crystal.**

423 Time traces of Bragg peaks intensities of {220}{310} {400} {330} {530} {800} {550} {750} and
424 {1020} for DJ n=2 crystal under 2 laser fluences: 1mJ/cm^2 (orange) and 2mJ/cm^2 (blue),
425 corresponding to injected carrier density of 1.3×10^{13}cm^{-2} and 2.5×10^{13}cm^{-2}, respectively.

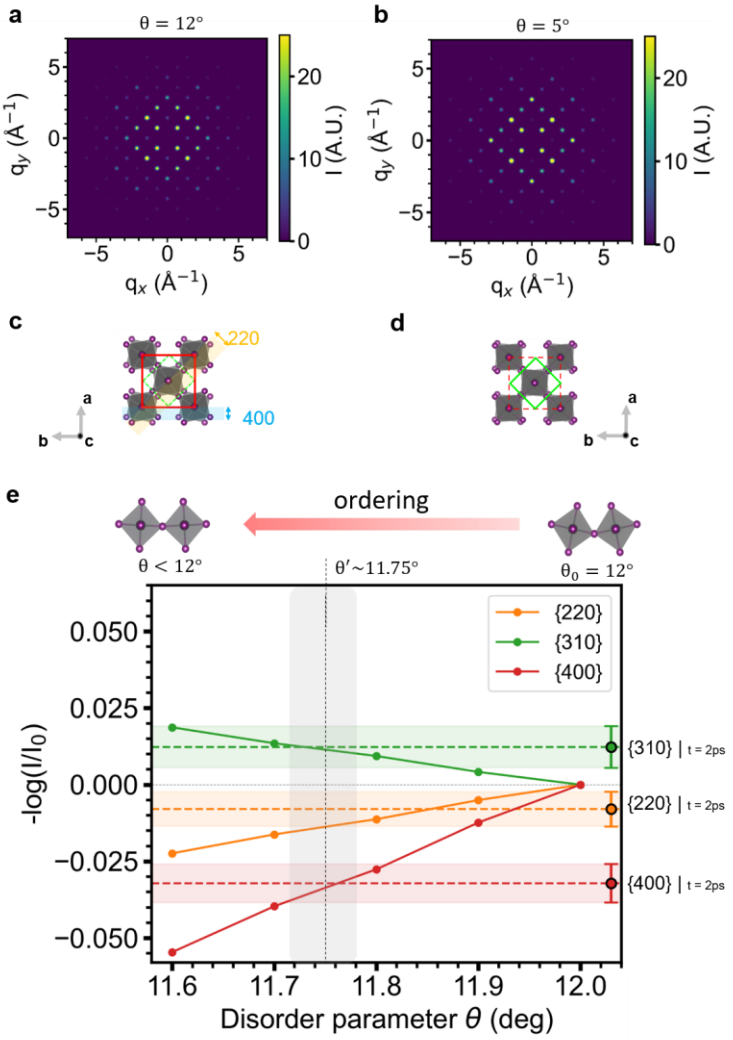

426

427 **Fig. S5 | Simulated Diffraction Patterns with tuned antiferro-distortion. (a)** Simulated
428 Diffraction of DJ n=2 at rest with intrinsic antiferro-distortion (θ=12^o). **(b)** Simulated Diffraction
429 of DJ n=2 with reduced antiferro-distortion (θ=5^o). **(c)(d)** Corresponding schematics of distorted
430 (θ=12^o) and less distorted phase (θ<12^o), respectively. **(e)** Simulated logarithmic intensity change
431 (-log(I/I$_0$)) for selected Bragg peaks as a function of disorder parameter θ, shown for {220} {310}
432 and {400} peaks (orange, green, and red solid lines), respectively. Compared with experimental
433 data (DJ n=2, 2.6×10^{13} cm^{-2}) at t=2ps (scattered points at right), the optimal change of disorder
434 parameter is estimated to be Δθ ~ 0.25^o (regime indicated in gray shadow).

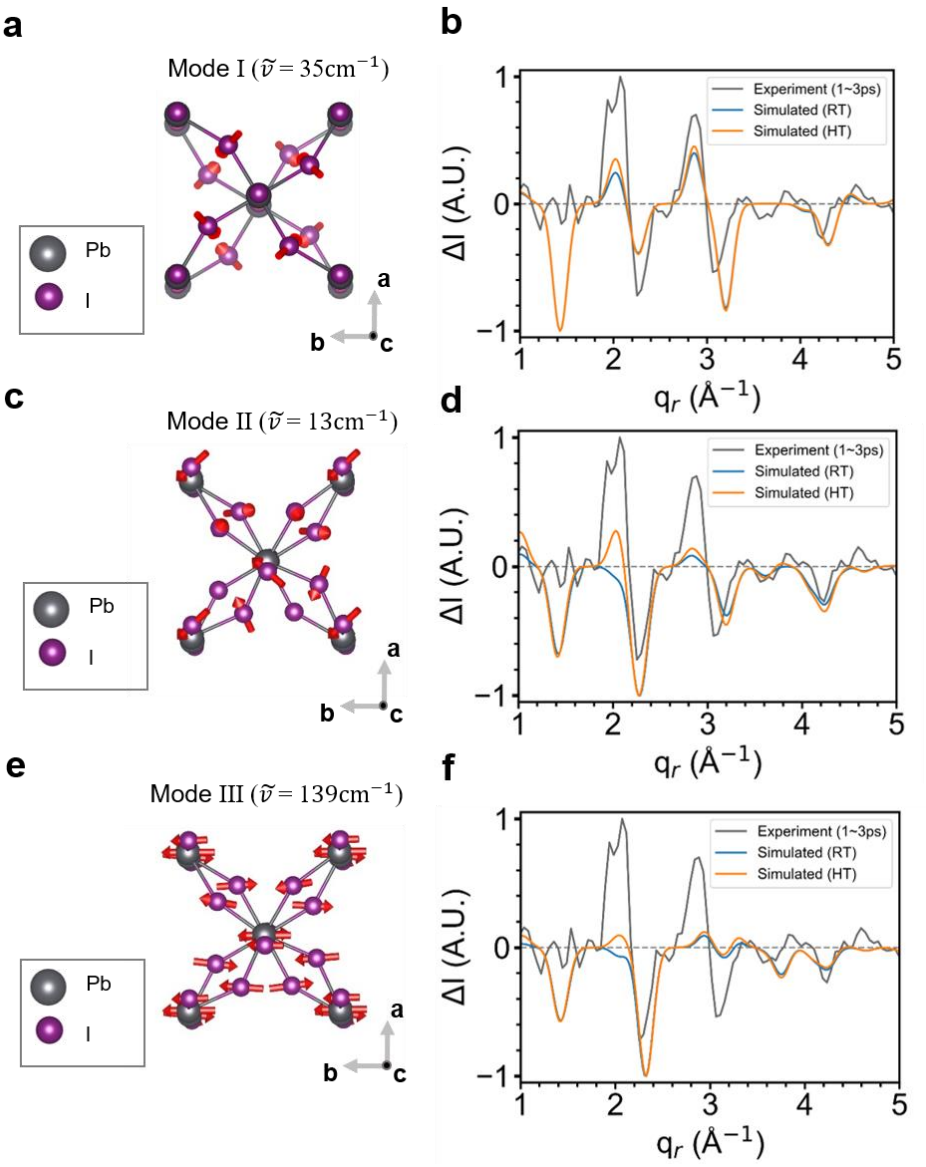

Fig. S6 | Examples of calculated antiferro-distortive phonon modes candidates in DJ n=2 crystal. (a)(c)(e) Schematic illumination of calculated normal modes (I, II and III respectively) acquired from phonon simulation (cations are neglected for visualization). The calculated wavenumbers are 35, 13, 139cm^{-1}, respectively. The directions of the atomic displacements are indicated with red arrows, suggesting a modulation of antiferro-distortions. **(d)(e)(f)** Simulated changes of electron diffraction plots for normal mode I, II and III respectively, estimated under room temperature (RT, blue solid line) and high temperature (HT, orange solid line) regimes. These simulated plots are compared with differential diffraction plot from UED experiment (1-3 ps, gray solid line), showing consistent peak increase at (220) and (400).

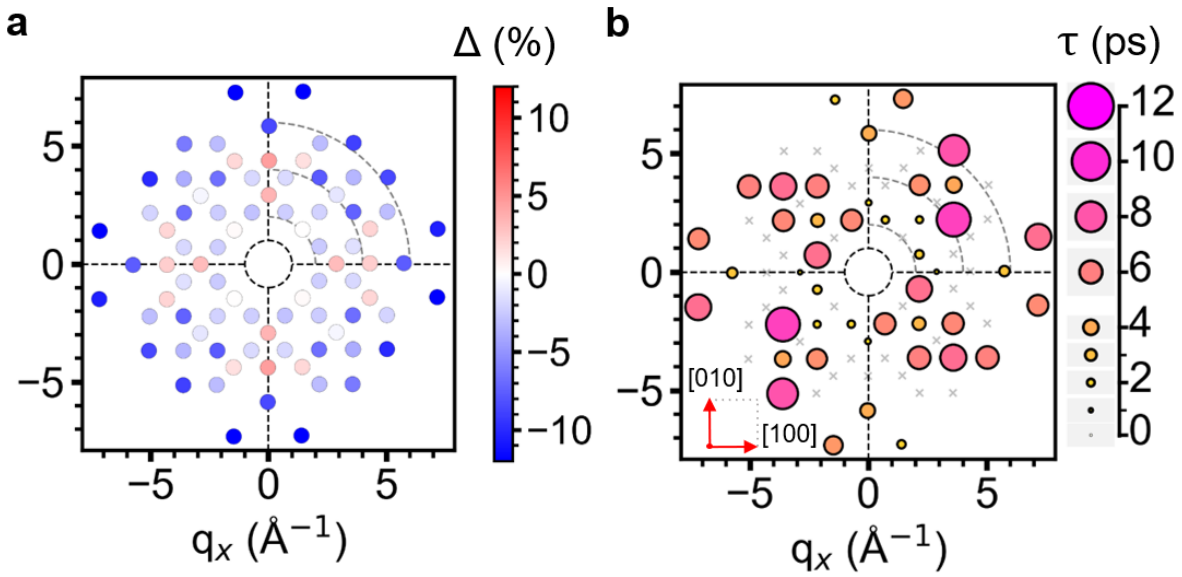

Fig. S7 | Scatter plots of fitted intensity change and time constants of DJ n=2 crystal. (a) Scatter plots of fitted intensity change (Δ (%)) of the Bragg peaks (hk0). Each Bragg peak (hk0) is averaged with (-h-k0) based on point symmetry. **(b)** Scatter plots of fitted time constant of the Bragg peaks, represented in both color scale and circle size (small and orange circles for short time, and large and pink circles for long time). 'x' markers stand for the Bragg peaks that cannot be well fit.

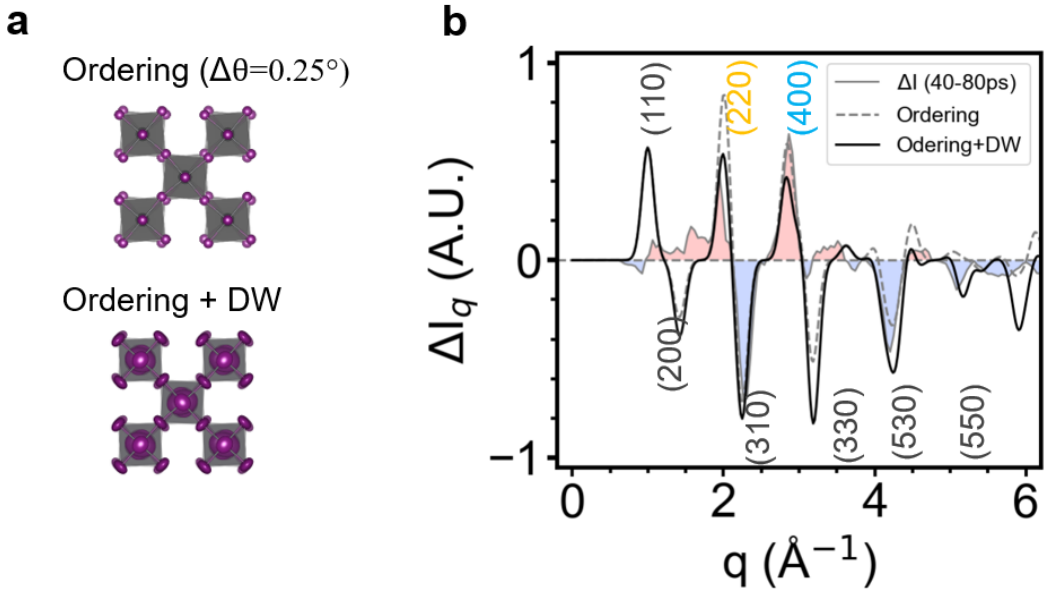

454

455 **Fig. S8 | Simulation of total UED response of DJ n=2 crystal. (a)** Simulated crystal structure
456 (top view) for different simulation methods: lattice ordering by reducing distortion angle (top),
457 and additional disorder involving all atoms (bottom). **(b)** Angular integrated differential diffraction
458 plot, averaged between 40-80 ps (gray solid line and shadow), compared with the simulated
459 response with only considering lattice ordering (gray dashed) and both ordering and Debye-Waller
460 effect (black solid line). The experimental intensity around the (110) peak is partially blocked.

461

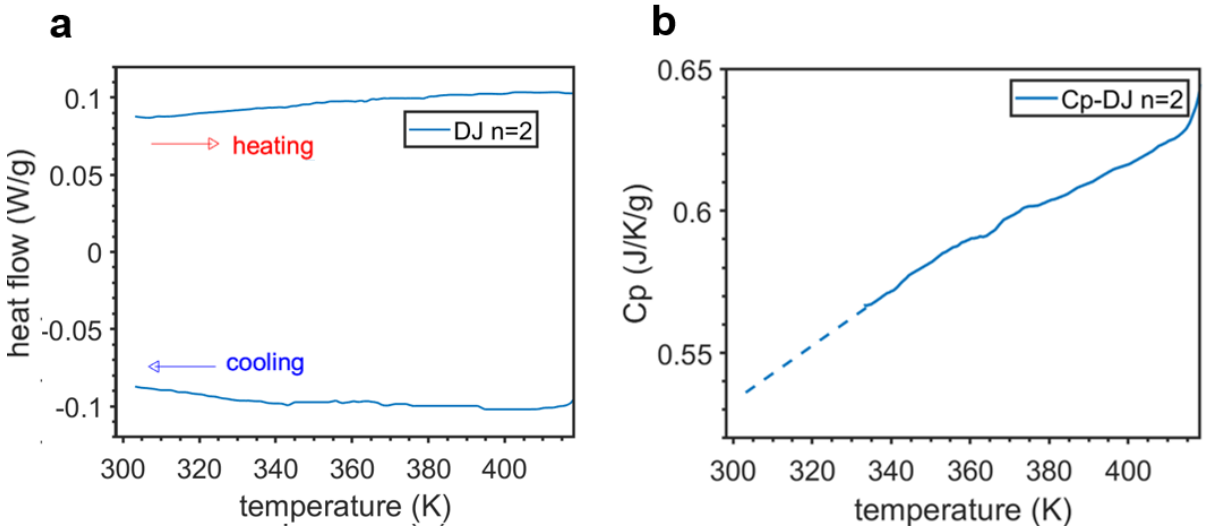

Fig. S9 | Differential scanning calorimetry (DSC) of DJ n=2 crystal. (a) DSC curve of DJ n=2 single crystals from room temperature to 150℃. **(b)** Calculated specific heat capacity (Cp) from DSC.

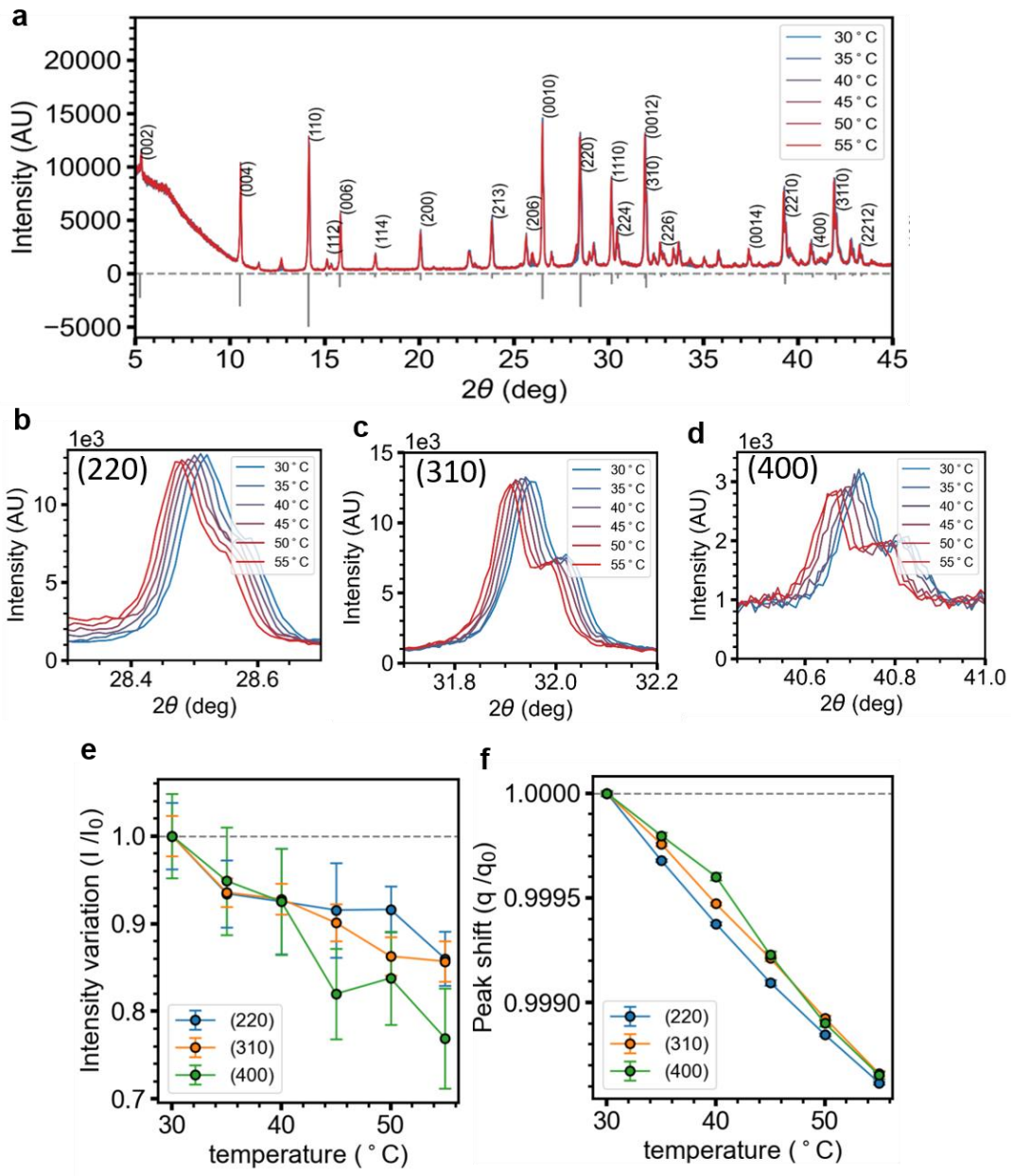

Fig. S10 | Temperature dependent XRD of DJ n=2 crystal. (a) Temperature dependent XRD from 30°C to 55°C. Simulated Bragg peak locations for DJ n=2 are indicated in vertical gray solid lines. **(b)(c)(d)** Zoomed-in XRD plots at in-plane peaks (220) (310) and (400) respectively, showing global shifting of peak locations (thermal expansion) and slight intensity decreases over temperature. **(e)** Analysis of relative intensity variation (I/I_0) and **(f)** relative peaks shift (q/q_0) for (220), (310) and (400) Bragg peaks. Error bars show the one standard deviation errors computed from the variance of the fitting parameters from least-squares fitting.

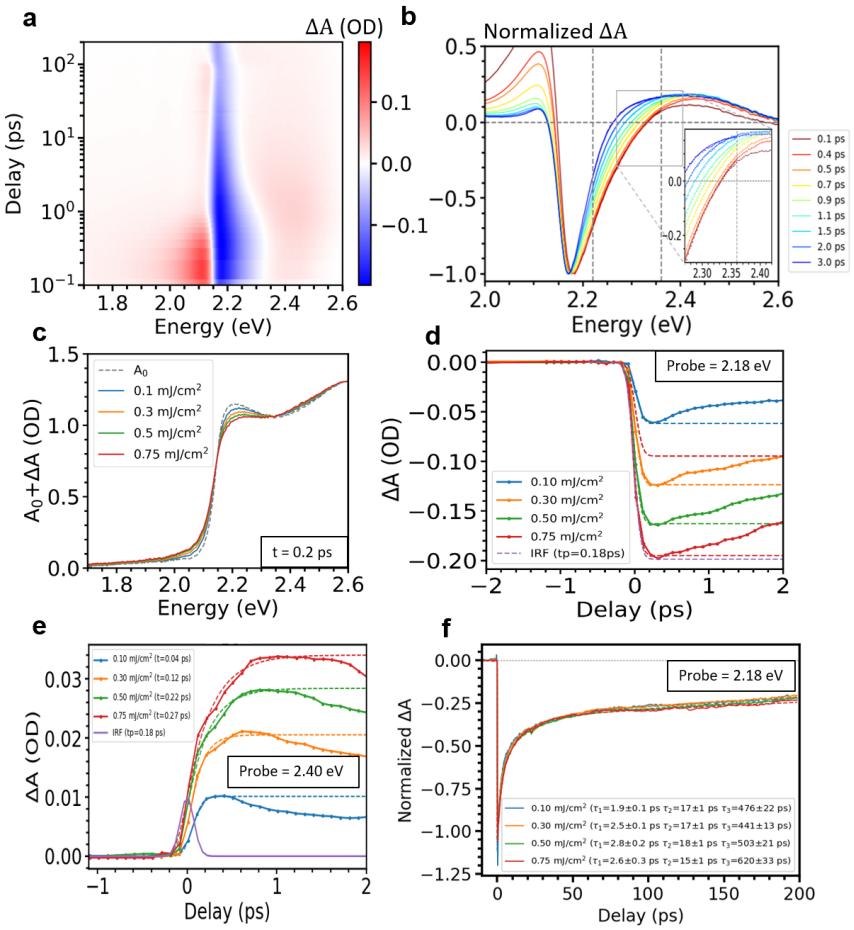

Fig. S11 | Transient absorption spectroscopy for DJ n=2 crystal. (a) Pseudo color representation of transient absorbance (Δ OD) as function of delay time, under 0.75mJ/cm^2. **(b)** Normalized TA spectra. The bleach amplitude at 2.18 eV is normalized to -1. High energy tails are fitted by Boltzmann distribution (black solid lines) to extract carrier temperature (shown in Fig. 3d). **(c)** Absolute absorption at various fluences, showing almost complete bleaching of exciton resonance. **(d)** Ultrafast bleaching ($\tau \leq 0.18$ ps) of exciton resonance at 2.18 eV, indicating fast ground state exciton bleaching after above-band excitation. **(e)** Evolution of TA dynamics at 2.40eV. The rise time is fitted with single exponential curve convolved with IRF (purple solid line), giving a rough estimation of carrier thermalization time. **(f)** Normalized exciton dynamics at 2.18eV, showing a long delay time (τ_3~10^2ps), suggesting a high density of electron-hole plasma still bleaches the exciton resonance at long time over 100-200ps. Fitting errors are estimated by the one standard deviation errors computed from the variance of the fitting parameters from least-squares fitting.

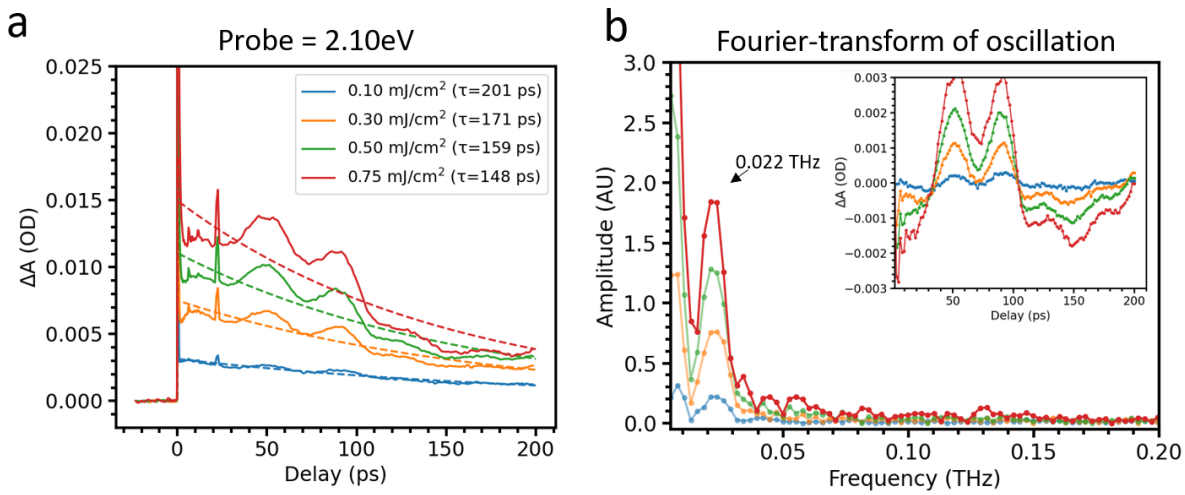

488

489 **Fig. S12 | Observations of coherent acoustic phonon in DJ n=2 and frequency analysis. (a)**
490 TA decay of probed at 2.10eV, showing oscillatory components with period T~45ps. **(b)**
491 Extraction of the oscillation (inset) and frequency domain analysis. Frequency below 0.0005THz
492 is discarded due to the limited window in temporal domain (≤ 200 ps).

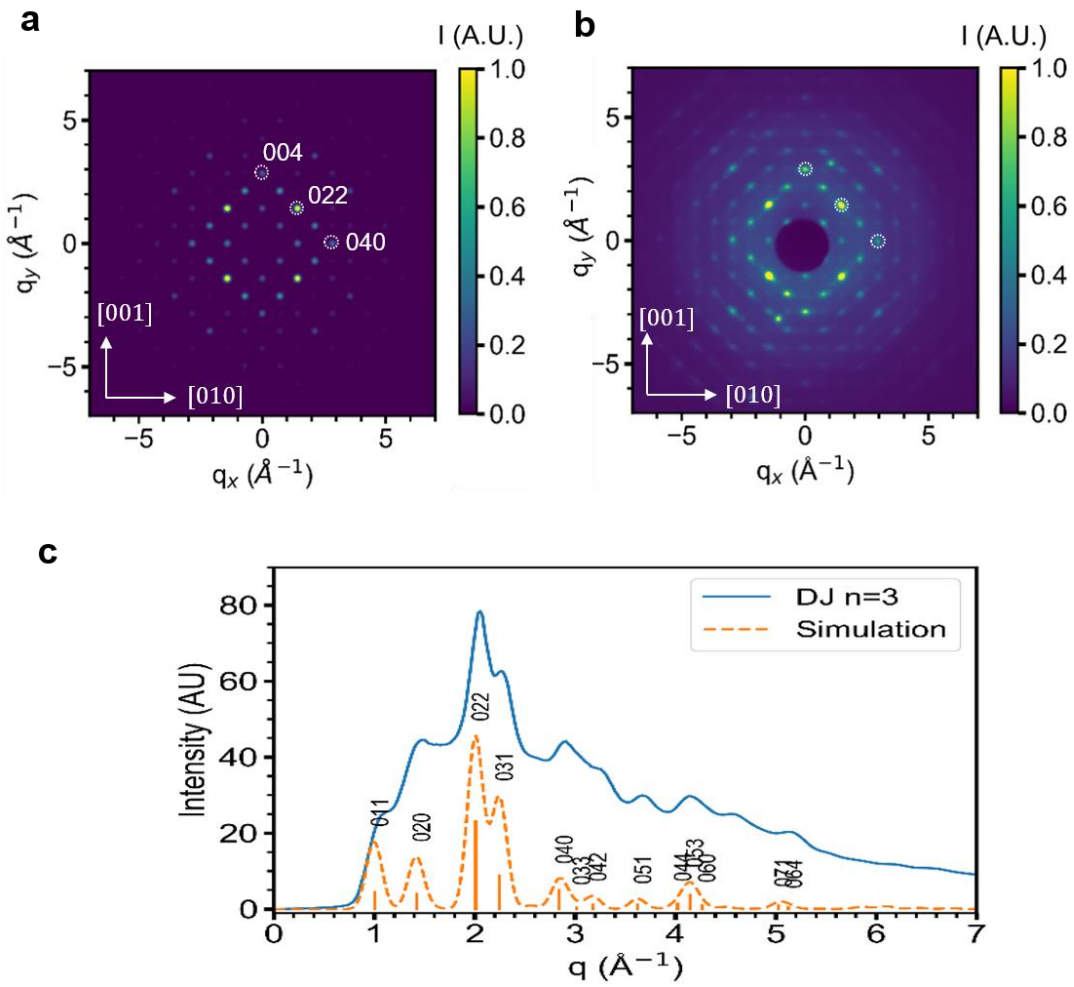

Fig. S13 | Simulated Diffraction Pattern & Indexing of DJ n=3 crystal.

(a) Simulated Diffraction of DJ n=3, viewing from [100] direction. **(b)** Static Diffraction of DJ n=3, showing same q-range as the simulated one in Fig. S13a. All the Bragg peaks are well-identified. **(c)** Angular-integrated diffraction of DJ n=3, showing both experimental (blue solid line) and simulated (orange dashed line) plots, as well as Indexing of Bragg peaks (0hk).

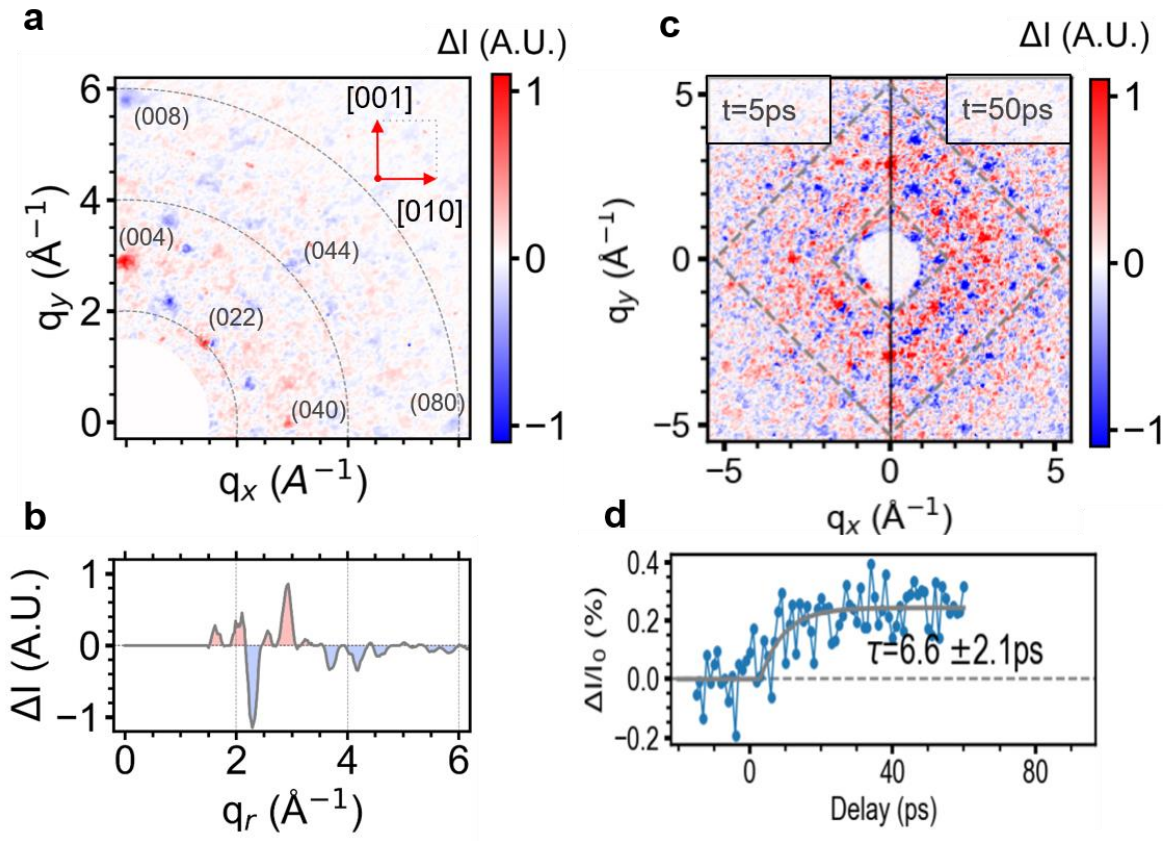

499

500 **Fig. S14 | Differential diffraction patterns of DJ n=3. (a)** Differential diffraction pattern (20-
501 40ps) for DJ n=3, showing similar response as DJ n=2, including the positively-changing peaks
502 (040), (022) and (004). **(b)** Angular-integrated differential diffraction (20-40ps) for DJ n=3. **(c)**
503 Differential diffraction pattern at 5ps (left) and 50ps (right). The increasing red colors in between
504 the peaks correlate to the diffuse scattering intensities. **(d)** Time traces of the integrated diffuse
505 scattering intensities integrated with the two squares in **(c).** Fitting errors are estimated by the one
506 standard deviation errors computed from the variance of the fitting parameters from least-squares
507 fitting.

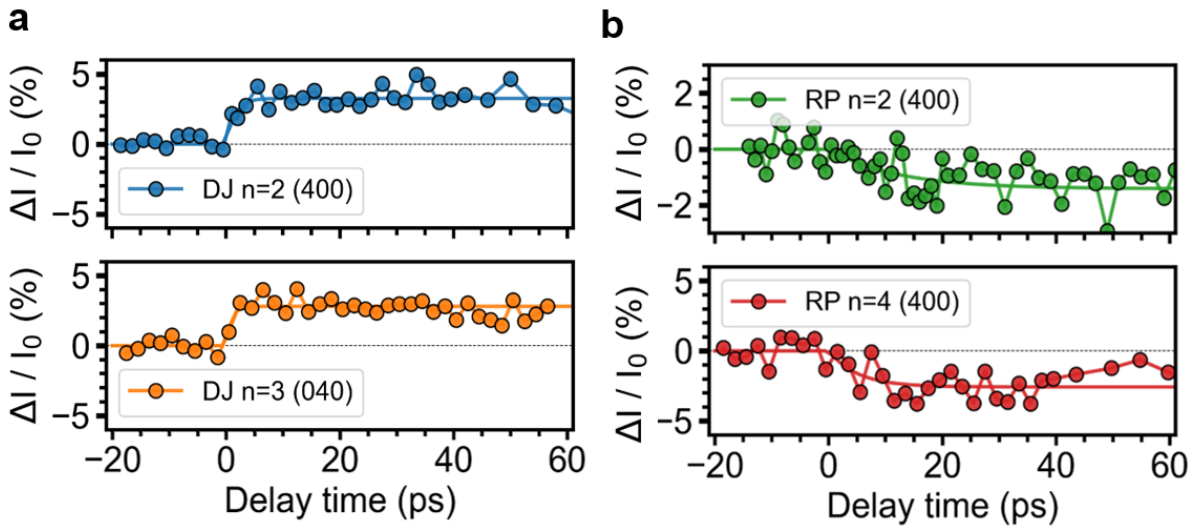

Fig. S15 | Comparison of time traces of selected Bragg peaks in 2D perovskites. (a) Time traces of DJ n=2 (400) (blue) and DJ n=3 (040) (orange) peak. Both peaks show a rapid increase in intensity. The rise-time constant fitted to be τ~1.3 ps (DJ n=2, blue solid line) and τ~0.9 ps (DJ n=3, orange solid line) respectively. **(b)** Time traces of RP n=2 (400) (green) and RP n=4 (400) (red) peak. Both peaks show a slower increase in intensity variations.

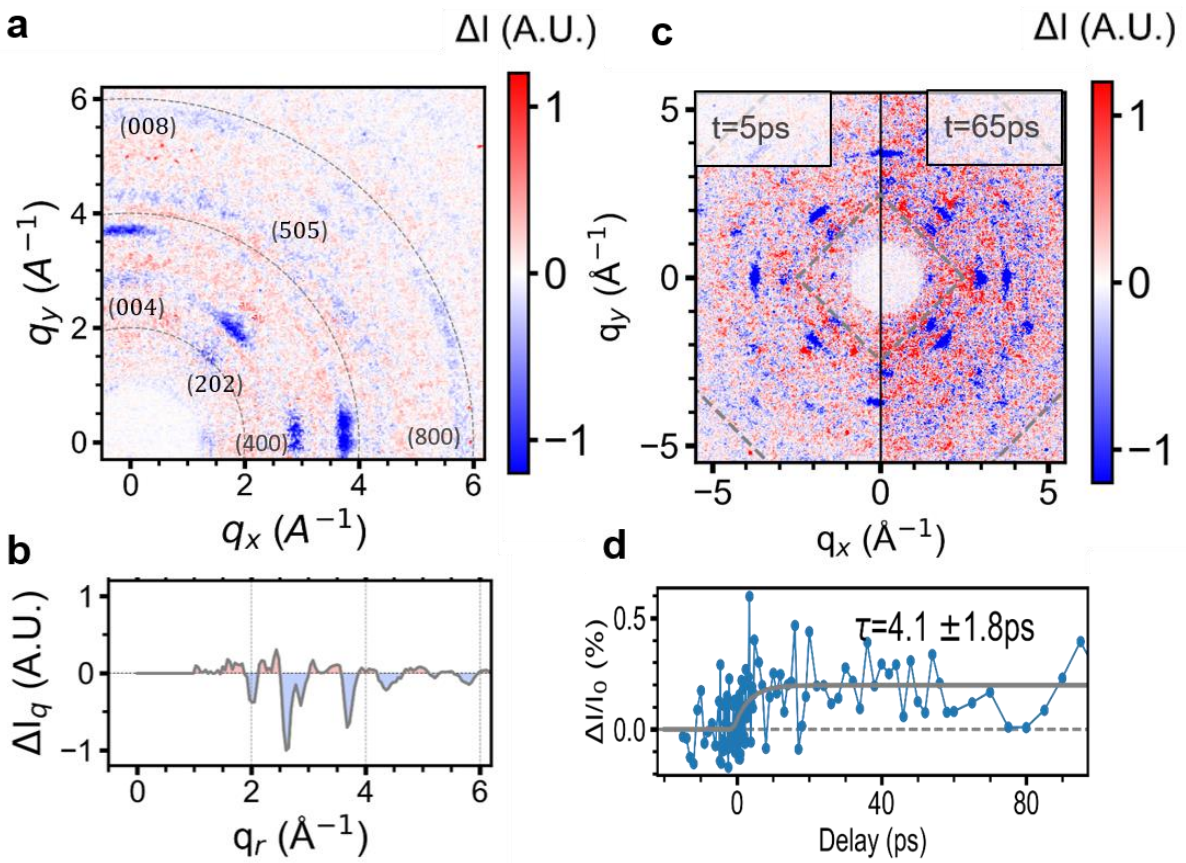

514

515 **Fig. S16 | Differential diffraction patterns of RP n=2. (a)** Differential diffraction pattern (15-
516 40ps) for RP n=2, showing different response than DJ samples where no peaks increasing observed.
517 **(b)** Angular-integrated differential diffraction (15-40ps) for RP n=2. **(c)** Differential diffraction
518 pattern at 2ps (left) and 65ps (right). The increasing red colors in between the peaks correlate to
519 the diffuse scattering intensities. **(d)** Time traces of the integrated diffuse scattering intensities
520 integrated in-between the two squares in **(c)** (dashed line). Fitting errors are estimated by the one
521 standard deviation errors computed from the variance of the fitting parameters from least-squares
522 fitting.

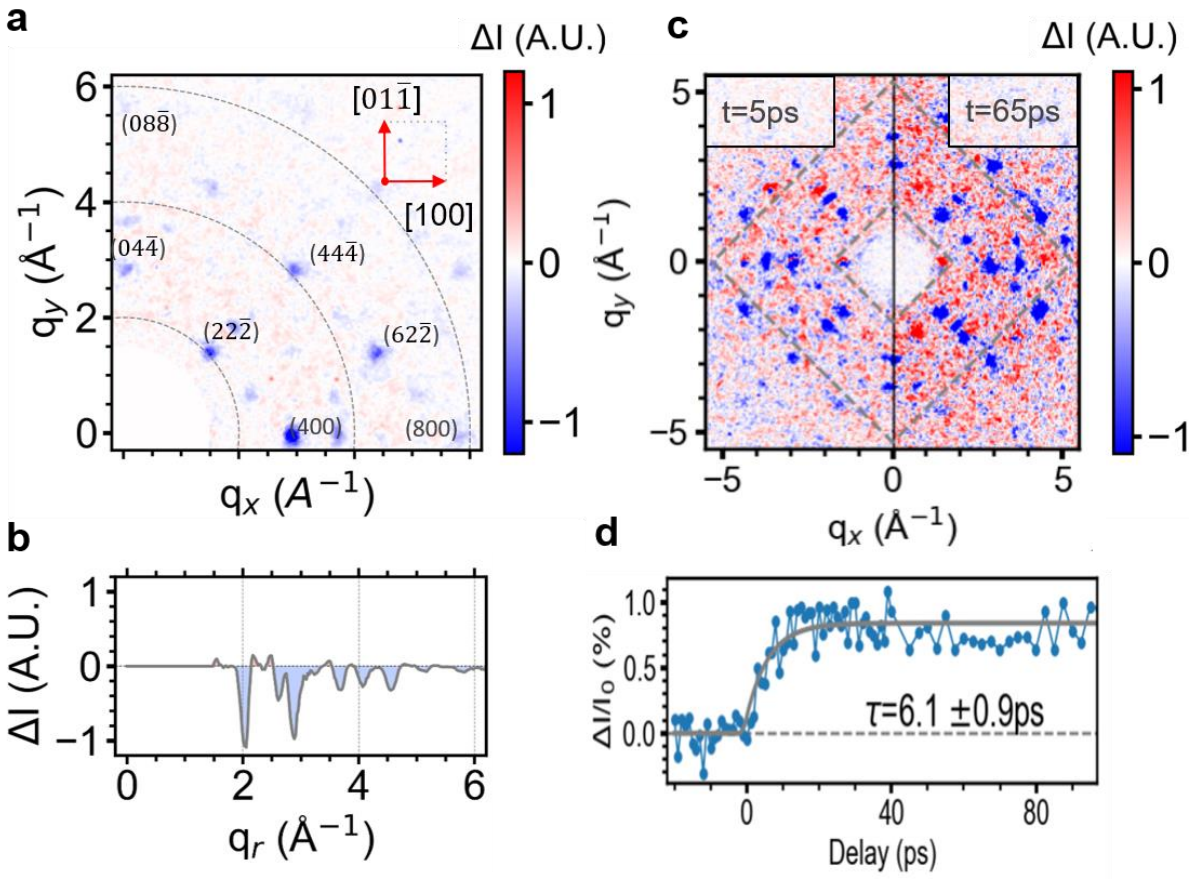

Fig. S17 | Differential diffraction patterns of RP n=4. (a) Differential diffraction pattern (20-40ps) for RP n=4, showing different response than DJ samples where no peaks increasing observed. **(b)** Angular-integrated differential diffraction (20-40ps) for RP n=4. **(c)** Differential diffraction pattern at 5ps (left) and 65ps (right). The increasing red colors in between the peaks correlate to the diffuse scattering intensities. **(d)** Time traces of the integrated diffuse scattering intensities integrated with the two squares in **(c).** Fitting errors are estimated by the one standard deviation errors computed from the variance of the fitting parameters from least-squares fitting.

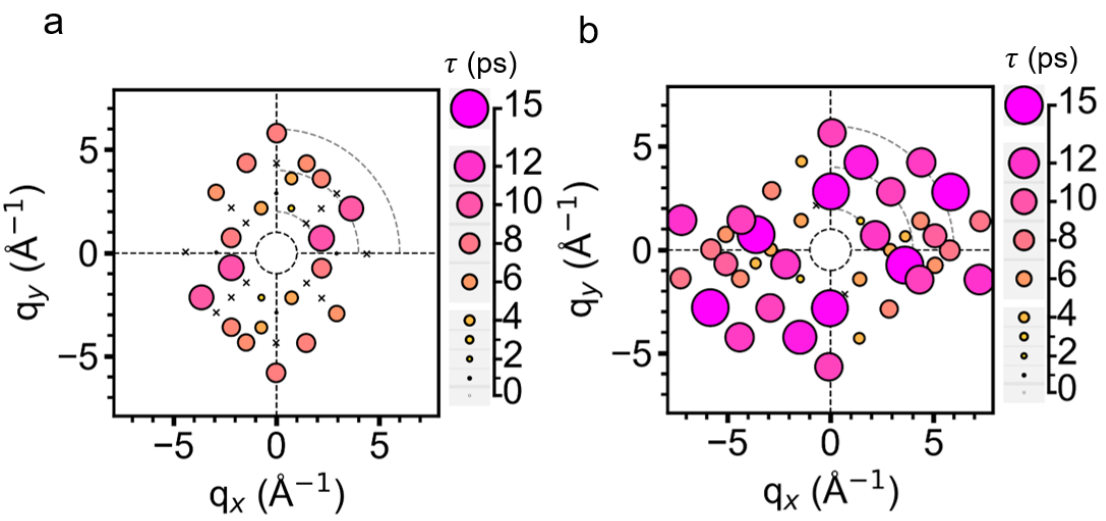

Fig. S18 | Time response comparison of different samples. Scatter plots of time constants (τ) of **(a)** DJ n=3 and **(b)** RP n=4 are shown. All the time constants are extracted from single exponential time fitting of Bragg peaks (averaged within each pair (hk0) and (-h-k 0)).

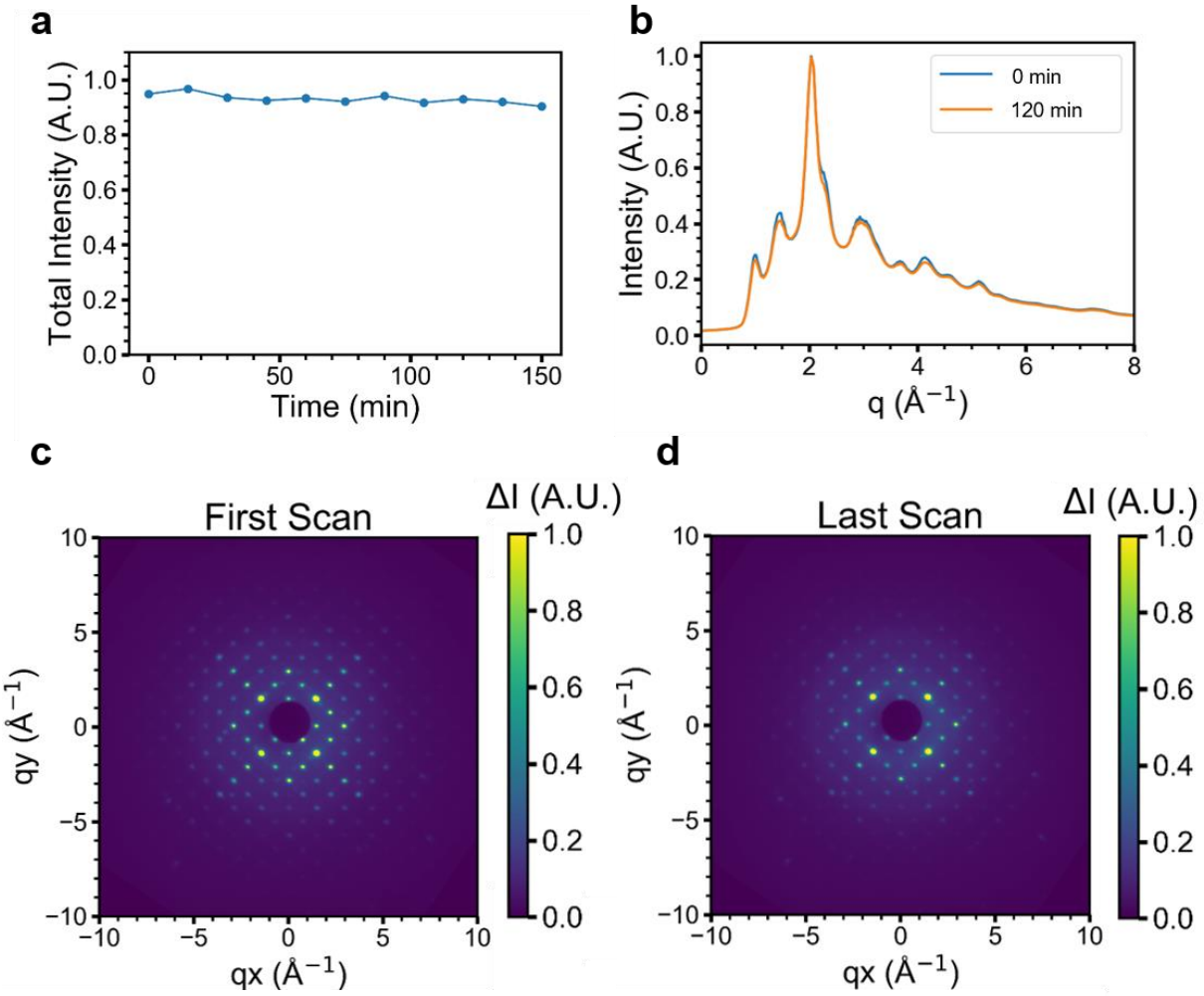

535

536 **Fig. S19 | Time Evolution of diffraction intensity of DJ n=2 crystal. (a)** Total electron
537 diffraction intensity during UED measurements over 150mins. **(b)** Azimuth integrated plot of
538 diffraction patterns taken at 0 min (blue) and 120mins (orange) after during the UED run. **(c)(d)**
539 Diffraction images of **(c)** first and **(d)** last scan.

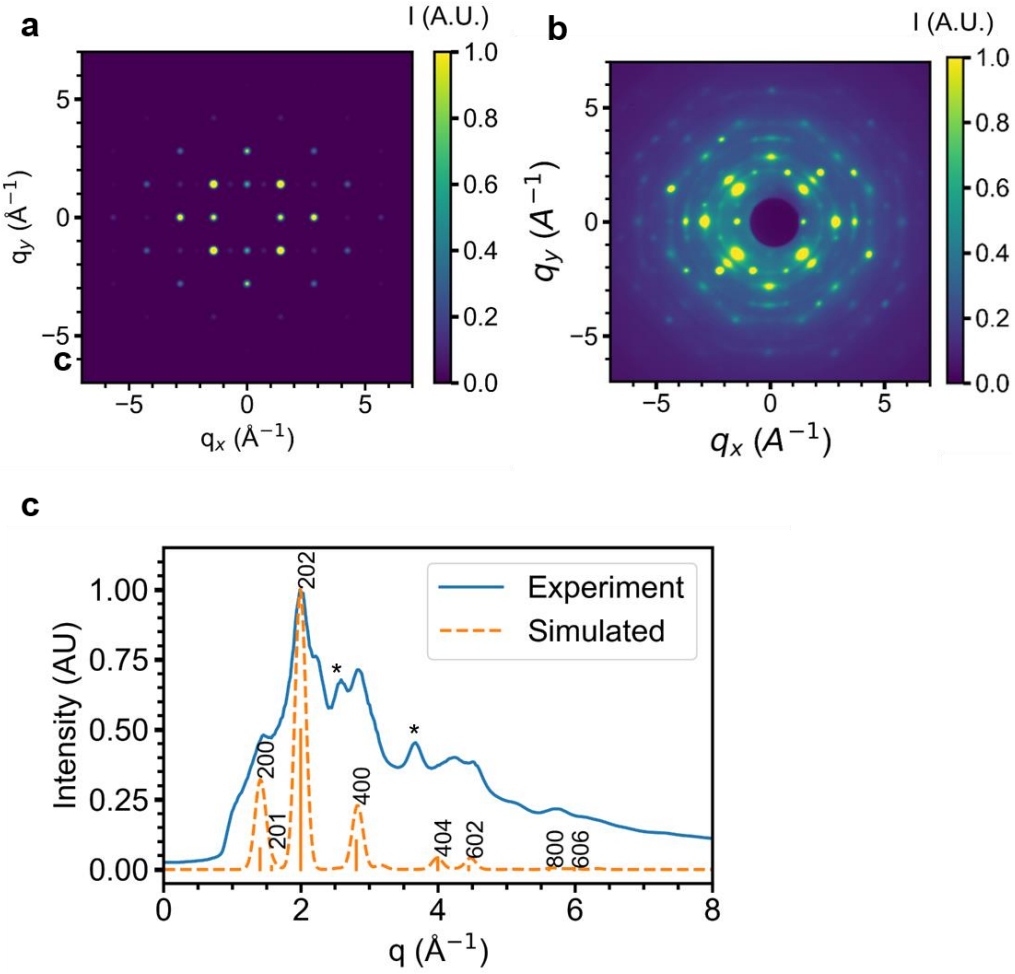

Fig. S20 | Simulated Diffraction Pattern & Indexing of RP n=2 crystal.

(a) Simulated Diffraction of DJ n=2, viewing from [010] direction. **(b)** Static Diffraction of RP n=2, showing same q-range as the simulated one in Fig. S20a. **(c)** Angular-integrated diffraction of RP n=2, showing both experimental (blue solid line) and simulated (orange dashed line) plots, as well as indexing of Bragg peaks (0hk).

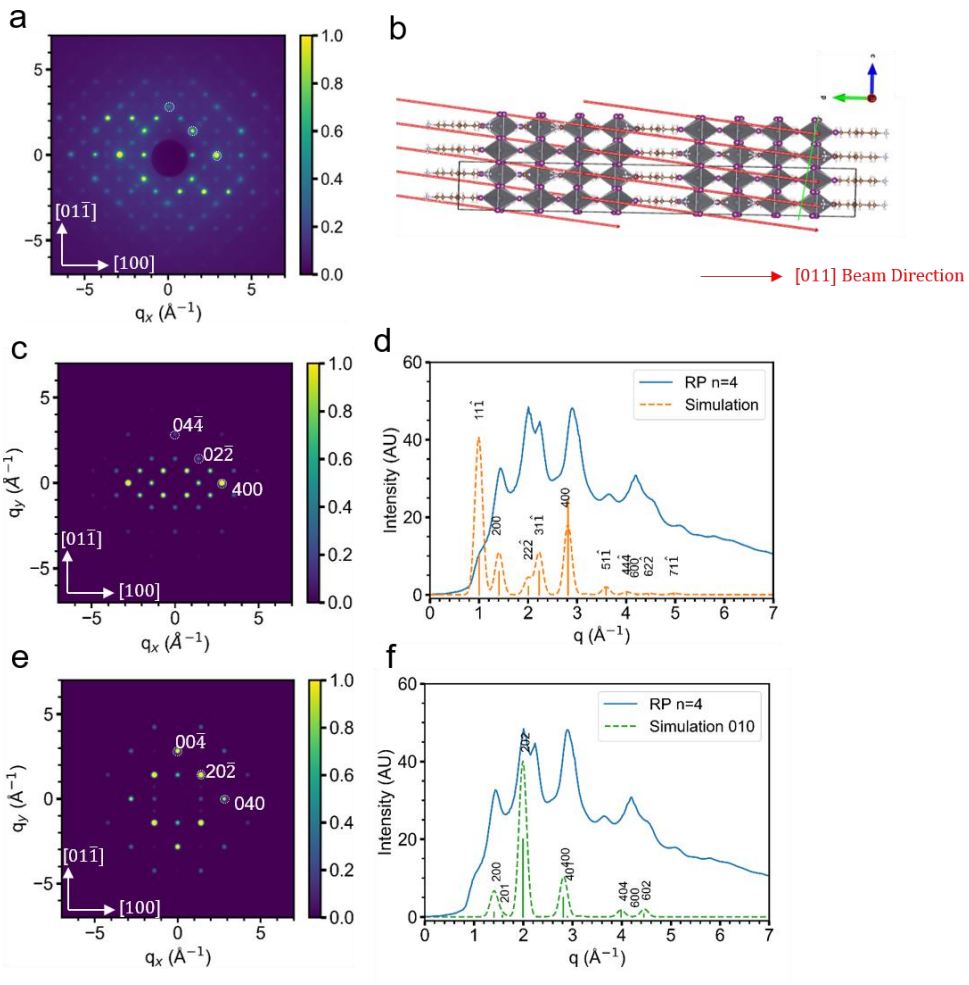

Fig. S21 | Simulated Diffraction Pattern & Indexing of RP n=4 crystal. (a) Static Diffraction patterns of RP n=4. **(b)** Schematics of RP n=4 and indication of [011] direction (red arrows). **(c)** Simulated Diffraction of RP n=4 along [011] direction. **(d)** Angular-integrated diffraction of RP n=4 viewing at [011], showing both experimental (blue solid line) and simulated (orange dashed line) plots, as well as Indexing of Bragg peaks. **(e)** Simulated Diffraction of RP n=4 along [010] direction, showing a mismatch with experimental patterns. **(f)** Angular-integrated diffraction of RP n=4 viewing at [010], showing both experimental (blue solid line) and simulated (green dashed line) plots, as well as Indexing of Bragg peaks.

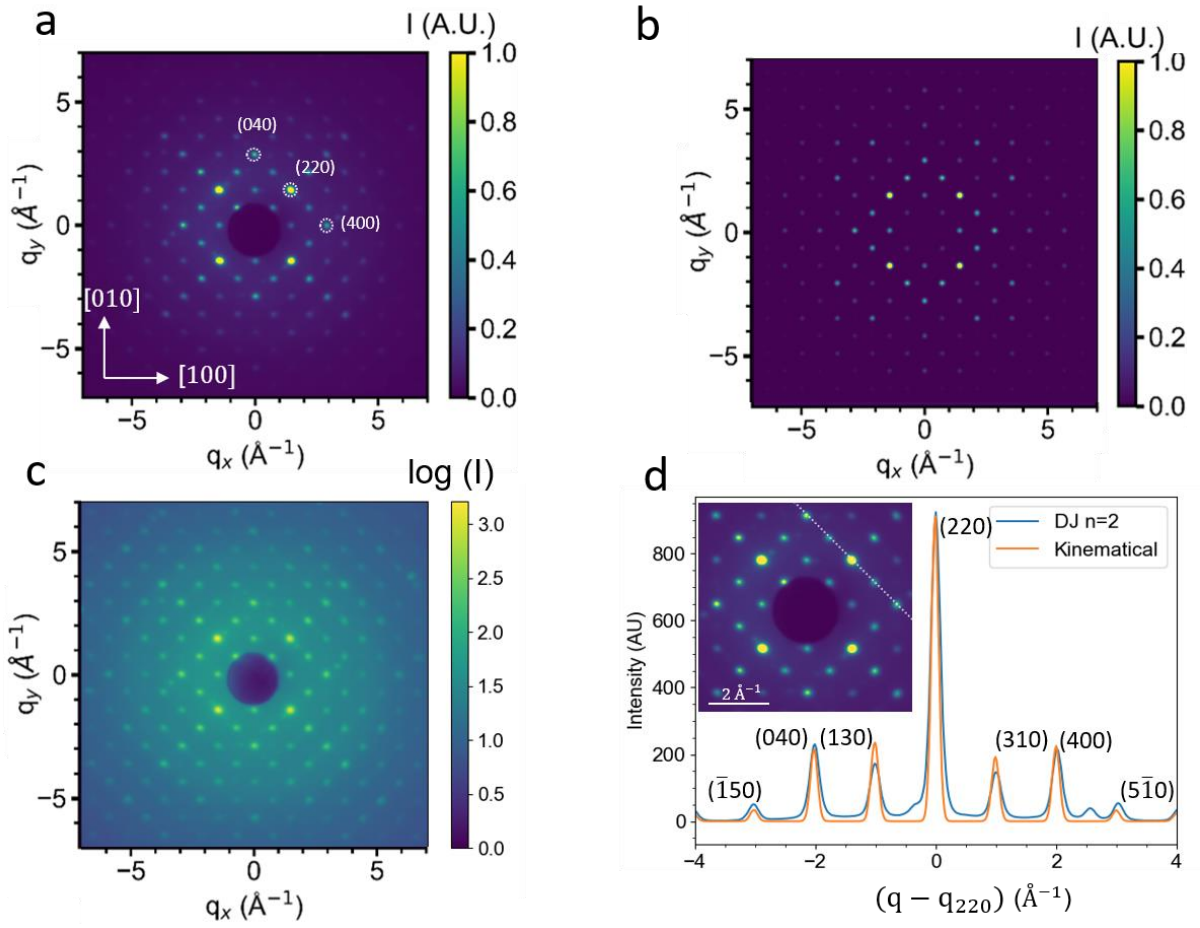

Fig. S22 | Comparison of the diffraction pattern of DJ n=2 with kinematical theory. **(a)** Static diffraction pattern of DJ n=2 crystal. **(b)** Simulated diffraction pattern with Kinematical scattering along c direction, computed from 4×4 supercell. **(c)** Logarithmic scale of the DJ n=2 diffraction pattern from (a), showing individual isolated Bragg peaks without Kikuchi lines. **(d)** Comparison of the linecuts of diffraction pattern along (040)-(040) direction (indicted by white dashed line in inset), showing consistent intensity distributions between experimental diffractions (blue) and the ones from kinematic theory (orange).

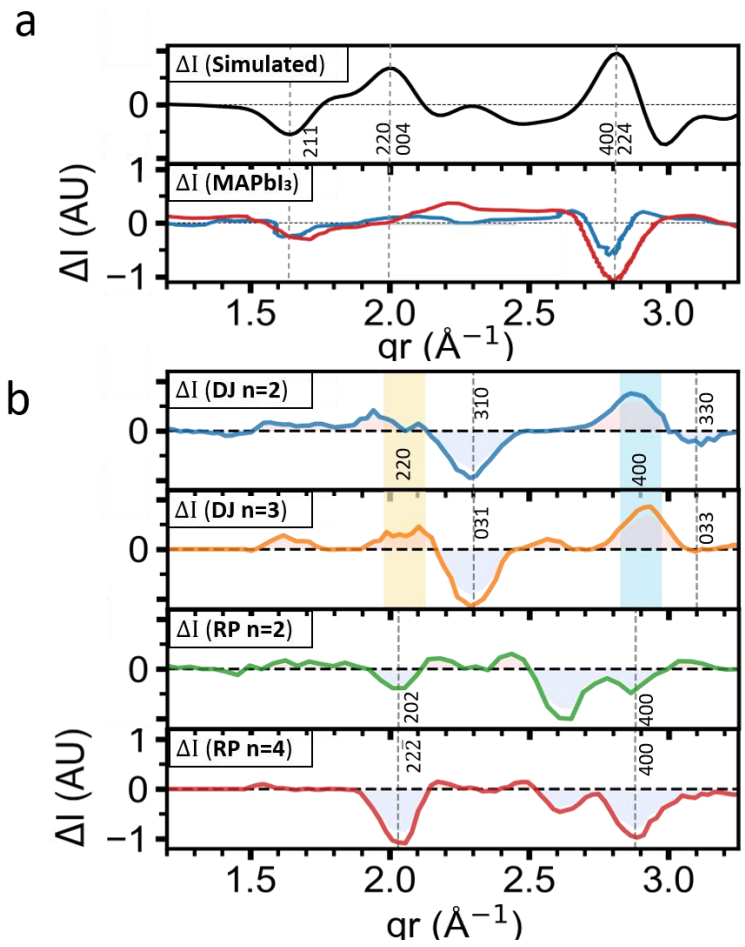

563

564 **Fig. S23 | Comparison of the angular-integrated diffraction of MAPbI3, with 2D DJ and RP**
565 **perovskites. (a)** The simulated differential diffraction pattern (black) is computed assuming a
566 complete reduction of the antiferro-distorsion present in the tetragonal phase of MAPbI3, leading
567 to a cubic lattice. The Bragg indices are assigned for the initial tetragonal structure. The simulation
568 is compared to the experimental differential diffraction curves of MAPbI3 for delay time t=5ps
569 (blue) and t=70ps (red) (Data extracted from Wu et al[1]). **(b)** Differential diffraction plots of 2D
570 perovskites reported in this work (Fig. 4c in manuscript).

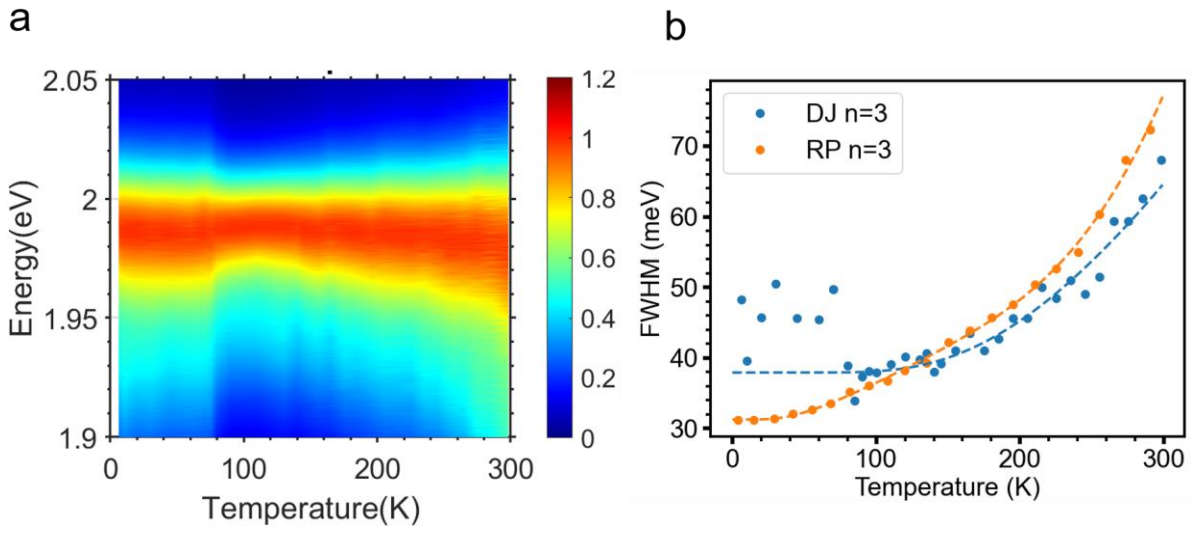

Fig. S24 | Temperature dependent PL on DJ and RP n=3 crystal. (a) Pseudo-colormap of PL as a function of temperature. **(b)** Extracted PL linewidth broadening, fitted with electron-LO phonon coupling model (dashed line).

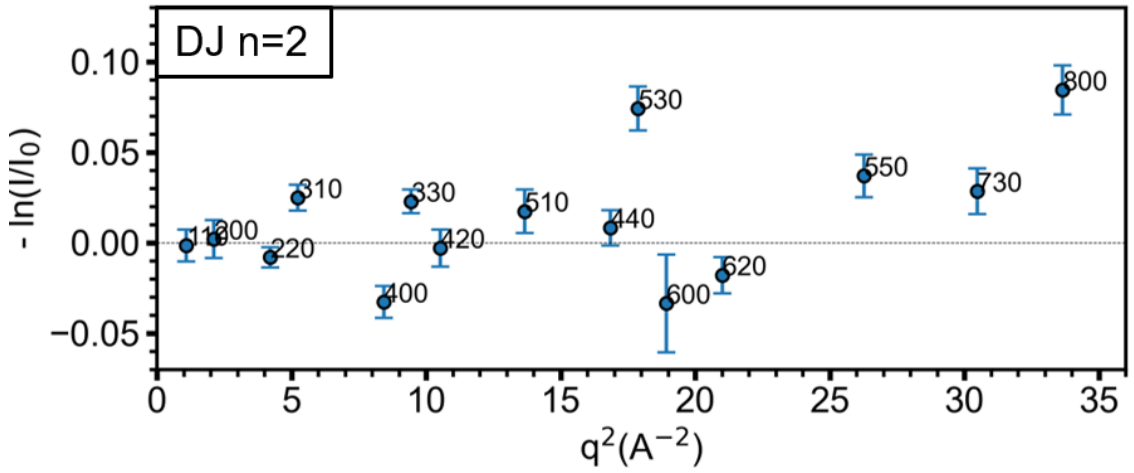

Fig. S25 | Semi-log plot of Bragg peaks intensity change as a function of q^2 for DJ n=2. Logarithmic plot of Bragg peaks total relative intensity change ($-\log(I/I_0)$) DJ n=2 under pump fluence energy of 2mJ/cm^2. Errors are estimated by the standard deviations of the intensity responses between 30 and 60ps (where quasi-equilibrium has been established for the Bragg peaks).

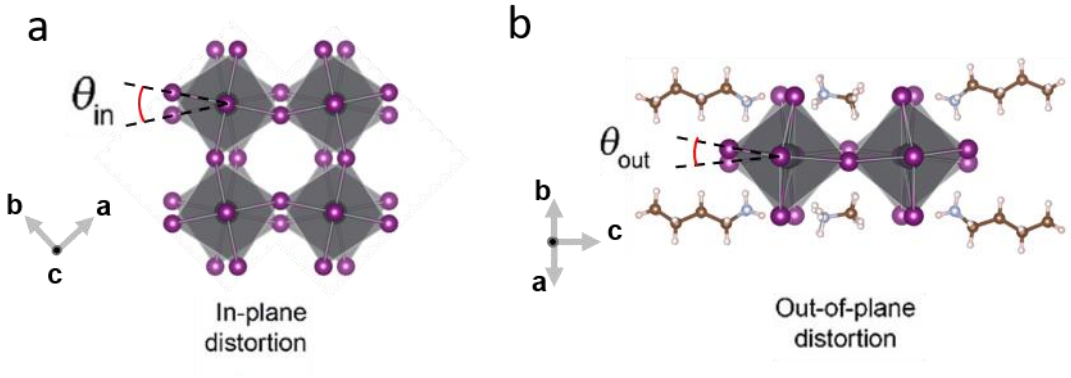

Fig. S26 | Illustration of in-plane and out-of-plane octahedral tilts. (a)(b) Definitions of the in-plane and out-of-plane octahedral tilts, respectively. A list of the octahedral tilts for measured perovskites is displayed in Table S2. The stacking axis of the 2D-HaPs is represented along c axis. The organics are not displayed in (a) for simplified visualization.

Supplementary Tables S1 - S2

Sample Name	DJ n=2	DJ n=3	RP n=2	RP n=4
Excitation Energy (eV)	3.1	3.1	3.1	3.1
Fluence (mJ/cm^2):	2	2.2	0.45	2.5
Crystal thickness (nm):	270	450	200	380
Optical density (at 3.1eV):	2.2	2.5	2.5	2.5
Carrier density (cm^{-2})	2.5×10^{13}	2.3×10^{13}	8.9×10^{12}	4.2×10^{13}

Table. S1 | Lists of experimental conditions of the measured samples: crystal thickness, excitation fluences and carrier densities. Sample thickness are estimated from the optical absorbance data in Fig. S1 for DJ n=2.

Sample Name	$(4AMP)Pb_2I_7$ (DJ n=2)	$(4AMP)Pb_3I_{10}$ (DJ n=3)	$(BA)_2PbI_2I_7$ (RP n=2)	$(BA)_2PbI_4I_{13}$ (RP n=4)	$MAPbI_3$	$SrTiO_3$ (< 1.5 K)	$KTaO_3$
Crystal system	Monoclinic	Monoclinic	Orthorhombic	Orthorhombic	Tetragonal	Tetragonal	Cubic
Structural phase	2D - DJ	2D - DJ	2D - RP	2D - RP	3D	3D	3D
Tilt (in-plane) (°)	11.78	11.2	0.02	0.03	/	/	/
Tilt (out-of-plane) (°)	0.72	0.46	7.66	6.42	/	/	/
Tilt (tetragonal axis) (°)	/	/	/	/	8.15	~2	0
Reference	3	3	4	4	13	27	32

Table. S2 | List of interlayer octahedral tilts (order parameter θ) for halide and oxide perovskites. The values are extracted from the corresponding crystal structures at room temperature (except for T<1.5K for $SrTiO_3$). For 2D perovskites, the octahedral tilts with in-plane (along stacking axis) vs out-of-plane (perpendicular to stacking axis) directions are distinguished (see Fig. S26). For 3D perovskites, similar tilt is defined along tetragonal axis.

References

1. Wu, X. *et al.* Light-induced picosecond rotational disordering of the inorganic sublattice in hybrid perovskites. *Science Advances* **3**, e1602388 (2017).
2. Song, B. *et al.* Determination of Dielectric Functions and Exciton Oscillator Strength of Two-Dimensional Hybrid Perovskites. *ACS Materials Lett.* **3**, 148–159 (2021).
3. Mao, L. *et al.* Hybrid Dion–Jacobson 2D Lead Iodide Perovskites. *J. Am. Chem. Soc.* **140**, 3775–3783 (2018).
4. Stoumpos, C. C. *et al.* Ruddlesden–Popper Hybrid Lead Iodide Perovskite 2D Homologous Semiconductors. *Chem. Mater.* **28**, 2852–2867 (2016).
5. Lin, M.-F. *et al.* Ultrafast non-radiative dynamics of atomically thin MoSe 2. *Nature Communications* **8**, 1745 (2017).
6. Ghosh, D. *et al.* Charge carrier dynamics in two-dimensional hybrid perovskites: Dion–Jacobson vs. Ruddlesden–Popper phases. *Journal of Materials Chemistry A* **8**, 22009–22022 (2020).
7. Gong, X. *et al.* Electron–phonon interaction in efficient perovskite blue emitters. *Nature Materials* **17**, 550–556 (2018).
8. Quan, L. N. *et al.* Vibrational relaxation dynamics in layered perovskite quantum wells. *PNAS* **118**, (2021).
9. Morrison, V. R. *et al.* A photoinduced metal-like phase of monoclinic VO2 revealed by ultrafast electron diffraction. *Science* **346**, 445–448 (2014).
10. González Vallejo, I. *et al.* Observation of large multiple scattering effects in ultrafast electron diffraction on monocrystalline silicon. *Phys. Rev. B* **97**, 054302 (2018).
11. Park, I.-H. *et al.* Self-Powered Photodetector Using Two-Dimensional Ferroelectric Dion–Jacobson Hybrid Perovskites. *J. Am. Chem. Soc.* **142**, 18592–18598 (2020).

12. Li, J. *et al.* Cs2PbI2Cl2, All-Inorganic Two-Dimensional Ruddlesden–Popper Mixed Halide Perovskite with Optoelectronic Response. *J. Am. Chem. Soc.* **140**, 11085–11090 (2018).
13. Stoumpos, C. C., Malliakas, C. D. & Kanatzidis, M. G. Semiconducting Tin and Lead Iodide Perovskites with Organic Cations: Phase Transitions, High Mobilities, and Near-Infrared Photoluminescent Properties. *Inorg. Chem.* **52**, 9019–9038 (2013).
14. Williams, D. B. & Carter, C. B. *Transmission electron microscopy: a textbook for materials science*. (Springer, 2008).
15. Peng, L.-M., Ren, G., Dudarev, S. L. & Whelan, M. J. Robust Parameterization of Elastic and Absorptive Electron Atomic Scattering Factors. *Acta Cryst A* **52**, 257–276 (1996).
16. Peng, L.-M. Electron Scattering Factors of Ions and their Parameterization. *Acta Cryst A* **54**, 481–485 (1998).
17. Kirkland, E. J. *Advanced Computing in Electron Microscopy*. (Springer US, 2010). doi:10.1007/978-1-4419-6533-2.
18. scikit-ued: (ultrafast) electron diffraction tools — scikit-ued 2.1.12 documentation. https://scikit-ued.readthedocs.io/en/master/index.html.
19. Otto, M. R. *et al.* Mechanisms of electron-phonon coupling unraveled in momentum and time: The case of soft phonons in TiSe2. *Science Advances* **7**, eabf2810 (2021).
20. Price, M. B. *et al.* Hot-carrier cooling and photoinduced refractive index changes in organic–inorganic lead halide perovskites. *Nat Commun* **6**, 8420 (2015).
21. Richter, J. M. *et al.* Ultrafast carrier thermalization in lead iodide perovskite probed with two-dimensional electronic spectroscopy. *Nature Communications* **8**, 376 (2017).
22. Yang, Y. *et al.* Observation of a hot-phonon bottleneck in lead-iodide perovskites. *Nature Photonics* **10**, 53–59 (2016).

23. Thouin, F. *et al.* Phonon coherences reveal the polaronic character of excitons in two-dimensional lead halide perovskites. *Nature Materials* **18**, 349–356 (2019).
24. Schmitt-Rink, S., Chemla, D. S. & Miller, D. A. B. Theory of transient excitonic optical nonlinearities in semiconductor quantum-well structures. *Phys. Rev. B* **32**, 6601–6609 (1985).
25. Blancon, J.-C. *et al.* Scaling law for excitons in 2D perovskite quantum wells. *Nature Communications* **9**, 2254 (2018).
26. Ishihara, T., Takahashi, J. & Goto, T. Optical properties due to electronic transitions in two-dimensional semiconductors (${\mathrm{C}}_{\mathit{n}}$${\mathrm{H}}_{2\mathit{n}+1}$${\mathrm{NH}}_{3}$ ${)}_{2}$${\mathrm{PbI}}_{4}$. *Phys. Rev. B* **42**, 11099–11107 (1990).
27. Kiat, J. M. & Roisnel, T. Rietveld analysis of strontium titanate in the Müller state. *J. Phys.: Condens. Matter* **8**, 3471–3475 (1996).
28. Radha, S. K., Bhandari, C. & Lambrecht, W. R. L. Distortion modes in halide perovskites: To twist or to stretch, a matter of tolerance and lone pairs. *Phys. Rev. Materials* **2**, 063605 (2018).
29. Bruce, A. D. & Cowley, R. A. Lattice dynamics of strontium titanate: anharmonic interactions and structural phase transitions. *J. Phys. C: Solid State Phys.* **6**, 2422–2440 (1973).
30. Akbarzadeh, A. R., Bellaiche, L., Leung, K., Íñiguez, J. & Vanderbilt, D. Atomistic simulations of the incipient ferroelectric $\mathrm{K}\mathrm{Ta}{\mathrm{O}}_{3}$. *Phys. Rev. B* **70**, 054103 (2004).

31. Wright, A. D. *et al.* Electron–phonon coupling in hybrid lead halide perovskites. *Nature Communications* **7**, 11755 (2016).
32. KTaO3 Crystal Structure: Datasheet from “PAULING FILE Multinaries Edition – 2012” in SpringerMaterials (https://materials.springer.com/isp/crystallographic/docs/sd_1412930).